Ordered motion in the turbulent boundary layer over wind waves

By H. KAWAMURA AND Y. TOBA

Department of Geophysics, Faculty of Science, Tohoku University, Sendai, 980 Japan

The turbulent boundary layer over young wind waves ($C/u_* \sim 1$, where C is the phase speed of wind waves and u_* is the friction velocity) has been investigated in a laboratory tank. Ordered motions have been found, and their structures studied in detail. Visualization of the outer boundary layer (0.4δ–1δ, where δ is the boundary-layer thickness) by paraffin mist has demonstrated the existence of a train of large-scale ordered motions having a horizontal lengthscale that corresponds to the wavelength of the underlying wind waves. Hot-wire measurements combined with the visualization have shown that the passage of the outer boundary-layer bulge is related to the occurrence of a low-speed air mass, usually accompanied by an upward velocity to produce large Reynolds stress. In the vicinity of the wave surface (0–0.15δ), flow separation occurs over these wind waves. Instantaneous velocity shear measurements, using two hot wires 0.15 cm apart vertically, have detected a high-shear layer at the edge of the separation bubbles. This high-shear layer, the potential site for generating much turbulence, reattaches on the windward side of the preceding wind waves. A pressure rise and a shear-stress spike, expected near the reattachment region, could be the mechanisms for supplying energy to the wind waves.

The bursting phenomena over wind waves have been examined in detail in the logarithmic boundary layer (0.15δ–0.3δ). The bursting phenomena are a major mechanism for producing Reynolds stress and have a specific relationship with the phase of the wind wave. To explain the bursting phenomena, two mechanisms (not present in the boundary layer over a flat plate) are proposed, involving air-flow separation and the large-scale ordered motions, respectively. The two mechanisms are a 'big burst' related to the discharge of a whole separation bubble, and a 'small burst' which is the upward bursting of a low-speed air mass from the unstable separated shear layer into the ordered motions passing over a separation bubble.

1. Introduction

In the last two decades there have been many experimental studies on turbulence in shear flows using direct flow measurements and flow visualization. These works have established the existence of ordered motions. After several important discoveries, it has been established that 'turbulent flows of single geometry are not so chaotic as has been previously assumed: there is some order in the motion with an observable chain of events reoccurring randomly with a statistically definable mean period' (Laufer 1975). The streaky structure (Kline *et al.* 1967; Kim, Kline & Reynolds 1971), the bursting phenomena (Corino & Brodkey 1969; Kim *et al.* 1971) and the coherent structure (Kovasznay, Kibens & Blackwelder 1970; Blackwelder & Kovasznay 1972) in the outer boundary layer have been connected with each other

to explain how turbulence is being generated and maintained in the turbulent boundary layer over flat plates. In his synthetical review of this new trend of turbulence studies, Cantwell (1981) has shown, in his figure 8, the similarities between three sketches, drawn by Blackwelder & Kovasznay, Falco (1977) and Brown & Thomas (1977), on the ordered motion over a plate. A fairly clear concept of the ordered motion has been given, as a recognizable large-scale structure. Grass (1971) has examined the turbulence structure over smooth, transitionally rough, and fully rough walls. He found that ejection (burst) and inrush (sweep) were present irrespective of the surface roughness conditions, and suggested that the bursting process could represent a universal and dominant mode of momentum transport outside the immediate wall region and possibly extending across the entire thickness of the boundary layer.

A number of researchers have pointed out that the turbulence structure over wind waves is somewhat similar to that over flat plates. A logarithmic law for the mean velocity profile, which was first established for the turbulent flow over solid plates, is now well established for the flow over wind waves in the laboratory. However, there are relatively few studies of the turbulent flow over wind waves from the point of view of the above-mentioned new trend of turbulence research. Takeuchi, Leavitt & Chao (1977) examined instantaneous Reynolds-stress in the air flow over the waves in a tank. Because of the use of mechanically generated water waves and low-wind conditions, the turbulent boundary layer in the cases studied had not developed sufficiently to investigate the constant-flux layer associated with the logarithmic profiles of the mean flow. It was shown by the classification of events producing the Reynolds stress that the events were more vigorous in the presence of the large-amplitude water waves than the flatter surface. Chambers & Antonia (1981) have analysed the velocity field in the atmospheric boundary layer above ocean waves for the range of $C/u_*\sim 33$–80 using the method of Lu & Willmarth (1973), where C is the phase velocity of waves and u_* the friction velocity. They have found that the probability that sweep and ejection associated with instantaneous shear-stress and heat-flux fluctuations occur at the same time is large and approximately independent of C/u_*. However, the probability of simultaneous occurrence of interaction events increases as C/u_* increases. Kawamura et al. (1981) have examined the turbulent boundary layer over wind waves in a tank by hot-wire anemometry and have shown that the statistical features of turbulence are very similar to those over flat plates. They have pointed out the existence of phenomena resembling the bursting phenomena over flat plates. However, there is at present no adequate description of the turbulent flow over wind waves to answer the question of how turbulence is generated and maintained. One of the primary motivations of this study is to investigate the air flow over wind waves with reference to the aspects of the ordered motions.

Detailed studies of turbulent boundary layers, including ordered motions, above and below wind waves must be essential for the elucidation of the dynamics of wind waves themselves, a key process in air–sea interactions. In fact, the existence of similarity laws of wind waves has already been proposed (e.g. Toba 1972, 1973, 1978), to represent the strong coupling of wind waves and turbulence in the air and water; the dynamical basis for these, however, is not yet established and requires detailed studies of the elementary processes involved.

Beginning with those of Toba et al. (1975), a series of experimental studies has been conducted by our group at Tohoku University, with an intention of directly observing the turbulent and irrotational part of the wind and the wind waves by
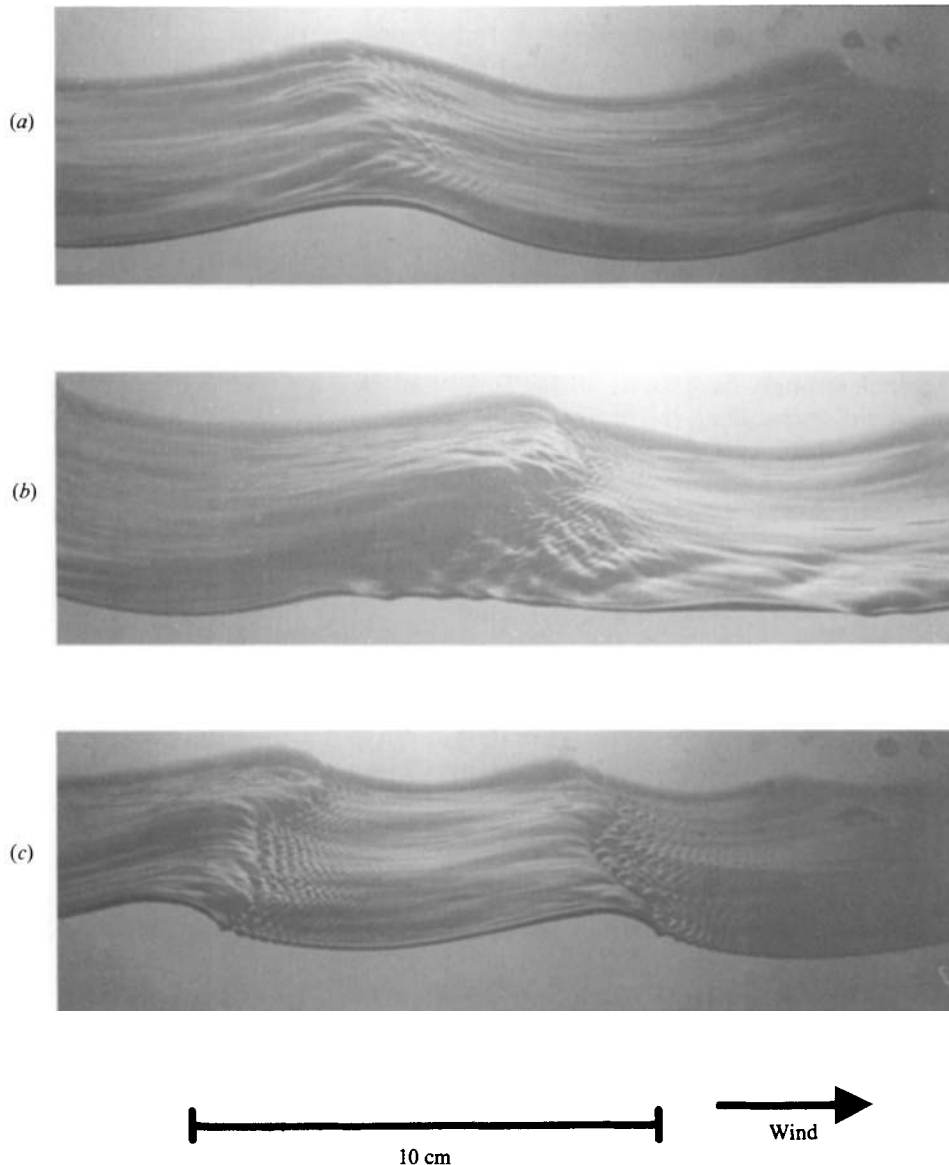
FIGURE 1. Photographs of wind waves at fetch = 6 m under wind speed U_1 ($U = 5.75$ m/s at the centre of the tunnel).

using flow visualization. Okuda, Kawai & Toba (1977) and Okuda (1982a) have investigated the turbulent water flow structure under wind waves using hydrogen bubbles and found a high-vorticity layer near the wind-wave crest. This layer is not supported steadily at an individual wave crest but grows and attenuates while the wave progresses. Figure 1 shows photographs of typical wind waves observed in our wind-wave tunnel. Under this condition, no air entrainment by wave breaking is observed. The photograph (*a*) shows a rather smooth, sinusoidal shape of wind waves. By contrast, (*b*) and (*c*) show a characteristic shape of the wave crests accompanied by the high-vorticity layer as investigated by Okuda (1982a). Under wind and wind-wave conditions in which C/u_* is close to unity, this kind of

configuration of the wave crests with a smooth shape and steep leading edge can be observed frequently on the open ocean water surface. Banner & Phillips (1974) recognized the (b)- and (c)-type configurations as 'micro-breaking' and related this to their theoretical study on 'incipient' breaking.

Air-flow separation behind a wind-wave crest has been discussed in relation to a stagnation (convergence) point expected just downstream of the wave crest (Banner & Melville 1976; Okuda 1982b). Chang, Plate & Hidy (1971) have indicated that, on average, the air flow separates over the dominant laboratory wind waves $(C/u_* \sim 1)$. By using air-flow visualization techniques, Kawai (1981, 1982) has shown that air-flow separation exists over young wind waves together with the air-flow pattern along waves. A critical relation between the local maximum gradient of the forward face of wind waves and the separation has been reported by Kawai (1982), which strongly suggested another type of air-flow separation caused by a flow that could not curve along the steep gradient of the wave crest. He has conjectured a strong mutual interaction between the wind and wind waves, i.e. the local stress exerted on the water surface changes the nature of a wave crest, especially its form (like figure 1b, c) and, as a result, the air-flow structure over it changes drastically (that is, air-flow separation). Weissman (1981) has shown that flow separation occurs over short mechanically generated waves ($\sim$ 10 cm wavelength) under low-wind conditions ($\sim$ 1 m/s), namely $C/u_* = 4.8$–5.6.

In this paper, we investigate the turbulent boundary layer over wind waves in a wind-wave tunnel which is the same as Kawai (1981, 1982) and Okuda (1982a) used. Section 2 of this paper describes the basic experimental apparatus and §3 is devoted to the statistical features of the turbulent air flow. To understand the whole structure of the air flow over wind waves, three height ranges of the boundary layer were examined by three different types of experiments. The experiments and the experimental results for the layers 0.4δ–1δ, 0–0.15δ, and 0.15δ–0.3δ, where the thickness of the turbulent boundary layer is δ, are described in §§4, 5 and 6, respectively. Combining these results, we propose possible mechanisms occurring in the whole turbulent boundary layer for the dynamical interaction between the air flow and wind waves, including the ordered motions (§7).

2. Wind-wave tunnel, basic instruments and data processing

The experiments were done in the wind-wave tunnel shown in figure 2, 0.15 m wide, 0.7 m high and 8 m long with a water depth of 0.52 m. Large eddies and distortions of the mean velocity profiles in the air flow were eliminated by a honeycomb (numeral 2 in figure 2) and fine mesh grids (3) in the air inlet duct. A permeable-type wave absorber (7) was installed at the downstream end of the tank. Before the start of each experiment, the water surface was cleaned by overflowing the water under strong wind conditions.

An orthogonal Cartesian coordinate system (x, y, z) is used: x in the streamwise direction of the air flow, with $x = 0$ (or fetch = 0 m) at the upstream end of the water tank; z upward normal to the mean water surface $z = 0$; and y normal to the (x, z)-plane, with $y = 0$ at the centre of the tunnel. The velocity components $U + u(t)$, $v(t)$ and $w(t)$ are also defined in the x-, y- and z-directions, respectively, where U is the time-averaged and $u(t)$, $v(t)$ and $w(t)$ the fluctuating components. In this study, two velocity components $(U + u(t), w(t))$ at $y = 0$ have been measured and discussed. The statistical features of the turbulent air flow over wind waves, and their changes in
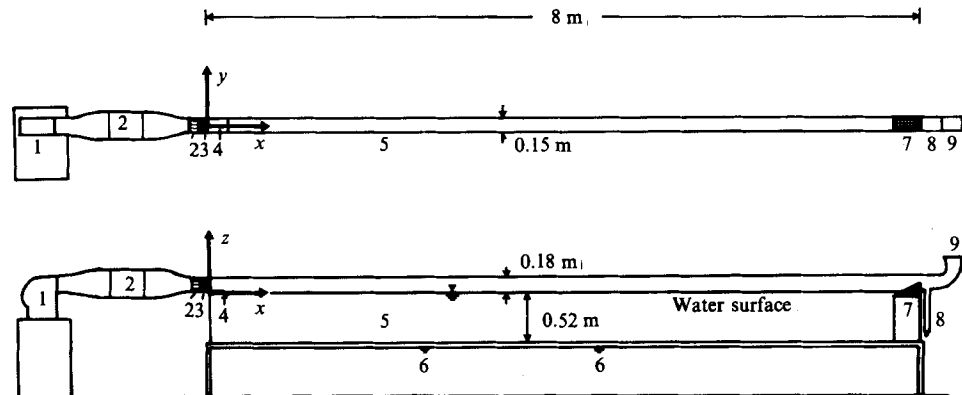
FIGURE 2. Schematic picture of the wind-wave tunnel. 1 fan, 2 honeycomb, 3 fine mesh grids, 4 guiding plate, 5 water tank, 6 water inlet (outlet), 7 wave absorber, 8 water outlet for water surface cleaning, 9 air outlet.

relation to the wind-wave growth, were measured in this wind-wave tunnel and have been described in detail by Kawamura *et al.* (1981, hereinafter called KOKT).

The experiments in the present study were carried out for two wind conditions: 5.75 m/s and 8.32 m/s at the centre of the tunnel at a fetch of 3.86 m, which are designated as U_1 and U_2, respectively.

The velocity fluctuations were measured by hot-wire and constant-temperature anemometers with linearizers. These measuring systems have frequency responses that are sufficiently rapid for the study of turbulent air flows. The linearized output voltages were calibrated frequently using a Pitot-static tube and a micromanometer during the measurement. Crossed hot wires, called an X-probe, were used to measure the velocity fluctuations, and the details of the method of deriving the velocity components from the X-probe output signals are described in KOKT. Several mean velocity profiles were measured by the Pitot-static tube and the micromanometer. Capacitance-type wave gauges were used to measure the surface displacement, $\eta(t)$. Hatori (1984) examined the frequency response of the wave gauge and concluded that it had sufficient sensitivity to determine fluctuations of the water surface up to 8 Hz.

The output signals of the hot-wire anemometers and the wave gauges were recorded on an analogue magnetic tape recorder and then digitized by an analogue-to-digital converter. The sampling intervals were 0.5 μs for the velocity fluctuations, and 5 ms for the surface displacements. The interval 0.5 μs, which is too short for the statistical analysis of the air flow, was selected in order to observe characteristic patterns of velocity fluctuations in this turbulent boundary layer. The 5-minute data for the velocity fluctuations and the 25-minute data for the surface displacements were digitized for the statistical analyses described in the next section.

3. Experimental conditions and statistical features of the turbulent boundary layer over wind waves

In §§4–6 turbulent motions in the air flow will be described from observations made by hot-wire anemometry and flow visualization. The experiment described in §4 was done at 3.86 m fetch under wind conditions U_1 and U_2, and the experiments

Wind	Exptmtl conditions	Fetch (m)	$\overline{\eta^2}$ (cm^2)	f_{p} (Hz)	$H_{\frac{1}{3}}$ (cm)	$T_{\frac{1}{3}}$ (s)	C (ms^{-1})	C/u_*
U_1	§4	3.86	1.12×10^{-2}	5.52	0.372	0.164	0.282	0.876
	§§5, 6	6.00	1.00×10^{-1}	3.86	1.07	0.251	0.404	1.38
U_2	§4	3.86	2.24×10^{-1}	3.61	1.76	0.274	0.432	0.933

TABLE 1. Statistical characteristics of wind waves. $\overline{\eta^2}$, mean-square amplitude; f_{p}, spectral peak frequency; $H_{\frac{1}{3}}$, significant wave height; $T_{\frac{1}{3}}$, significant wave period; C, phase speed of wind waves determined from f_{p} by applying the dispersion relation of gravity wave; u_*, friction velocity (see table 2).

Wind	Expmtl conditions	Fetch (m)	u_* (m/s)	z_0 (m)	U_∞ (m/s)	δ (cm)
U_1	§4	3.86	0.322	5.39×10^{-3}	5.75	6.1
	§§5, 6	6.00	0.293	1.49×10^{-2}	5.72	6.1
U_2	§4	3.86	0.463	6.40×10^{-3}	8.32	6.7

TABLE 2. Characteristic values of the turbulent boundary layer. u_*, friction velocity; z_0, roughness length; U_∞, free-stream velocity; δ, boundary-layer thickness.
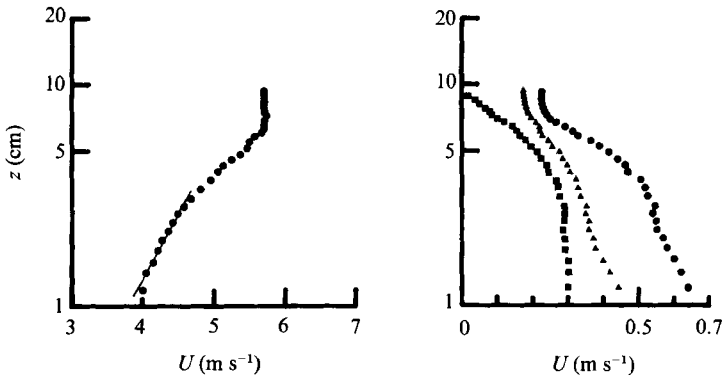

FIGURE 3. Profiles of the mean air velocity U, turbulence intensities $(\overline{u^2})^{\frac{1}{2}}$ (●), $(\overline{w^2})^{\frac{1}{2}}$ (▲), and Reynolds stress $(\overline{-uw})^{\frac{1}{2}}$ (■), obtained at fetch = 6 m at U_1. $u_* = 0.29$ m s^{-1}.

in §§5 and 6 were carried out at 6 m fetch under wind condition U_1. The mean-square amplitude of wind waves $\overline{\eta^2}$, the spectral peak frequency f_{p}, the significant wave height $H_{\frac{1}{3}}$ and period $T_{\frac{1}{3}}$ are listed for each case in table 1, together with the phase speed of waves C calculated from f_{p} and C/u_*.

In table 2 are listed the characteristic values of the turbulent air flow for each case, i.e. the friction velocity u_* and the roughness length z_0 (both obtained by applying the logarithmic law with von Kármán's constant 0.4), the free-stream velocity U_∞, and the boundary-layer thickness δ (the height where $U = 0.99U_\infty$).

Averaged features of the representative turbulent boundary layer over wind waves are shown in figure 3 for fetch = 6 m at U_1, which are the experimental conditions of §§5 and 6. The figure presents profiles of mean velocity, turbulence intensity $(\overline{u^2})^{\frac{1}{2}}$, $(\overline{w^2})^{\frac{1}{2}}$ and Reynolds stress $(\overline{-uw})^{\frac{1}{2}}$. A logarithmic layer can be seen in the lower part of the boundary layer. The friction velocity u_* of 0.29 m/s corresponds well with the
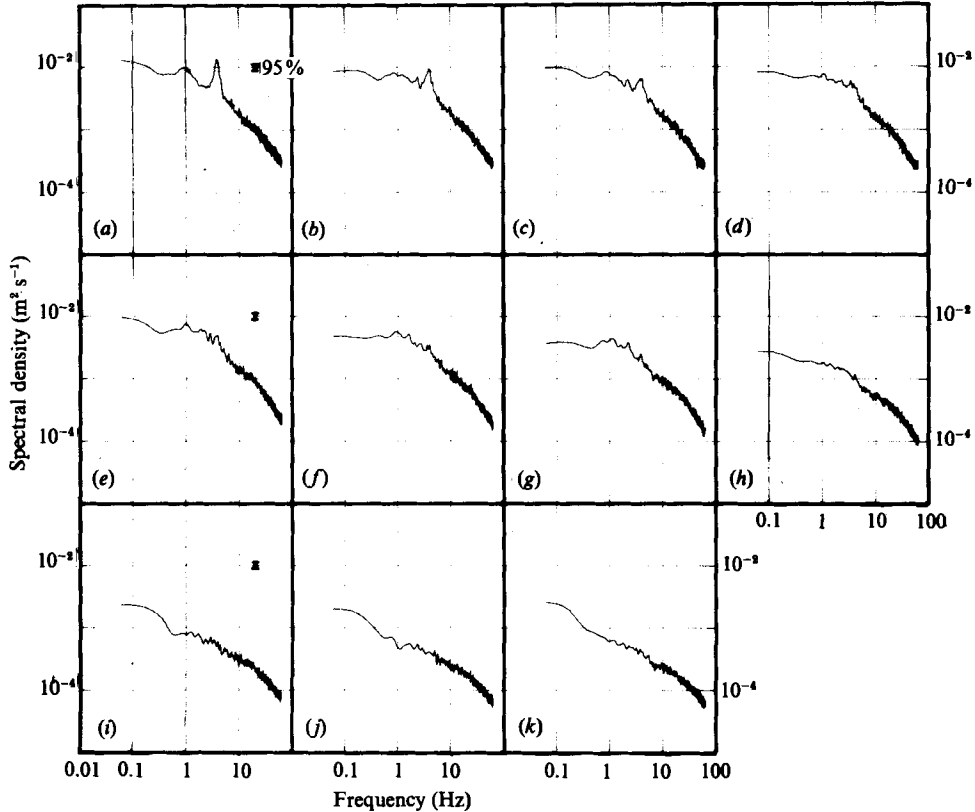
FIGURE 4. Power spectra of u at (a) $z = 1.2$ cm, (b) 1.6 cm, (c) 2.0 cm, (d) 2.4 cm, (e) 3.1 cm, (f) 4.0 cm, (g) 4.9 cm, (h) 6.1 cm, (i) 7.0 cm, (j) 7.9 cm and (k) 9.1 cm.

square root of the Reynolds stress measured by the hot wire in the logarithmic layer where the Reynolds stress is nearly constant. The turbulence intensity decreases with height and becomes a constant again around the tunnel core where the mean velocity is a constant (free-stream velocity) and the Reynolds stress becomes zero. The constant intensity in the core indicates nearly isotropic initial turbulence generated by the fine mesh grids at the air inlet. This region exists in the other cases. The normalized initial turbulence intensity $(\overline{u^2})^{\frac{1}{2}}/U$ is about 4% at the wind core at fetch $= 3$ m. These conditions are different from that of fully developed channel flow in which the whole section of the tunnel is filled with turbulence associated with the top wall and the bottom boundary. This is an important point to be considered in the expriment described in §4, in which we intend to observe the structure of the outer edge of the turbulent boundary layer over the wind waves. The fully developed condition of the wind-wave tunnel was discussed in KOKT using the velocity defect law for the turbulent boundary layer. Small increments of $(\overline{u^2})^{\frac{1}{2}}$ and $(\overline{w^2})^{\frac{1}{2}}$ with decreasing z are seen in the region near the water surface. According to KOKT, the increments depend on the flow components along the wavy undulations of the water surface.

Figures 4 and 5 show the power spectra of u and w, respectively. Each is an ensemble average of 70 raw spectra calculated from 4096 data points. The peaks at the characteristic frequency of the wind waves are seen in the lower elevations in both u- and w-spectra. In the logarithmic boundary layer $(a$–$d)$, the spectral density
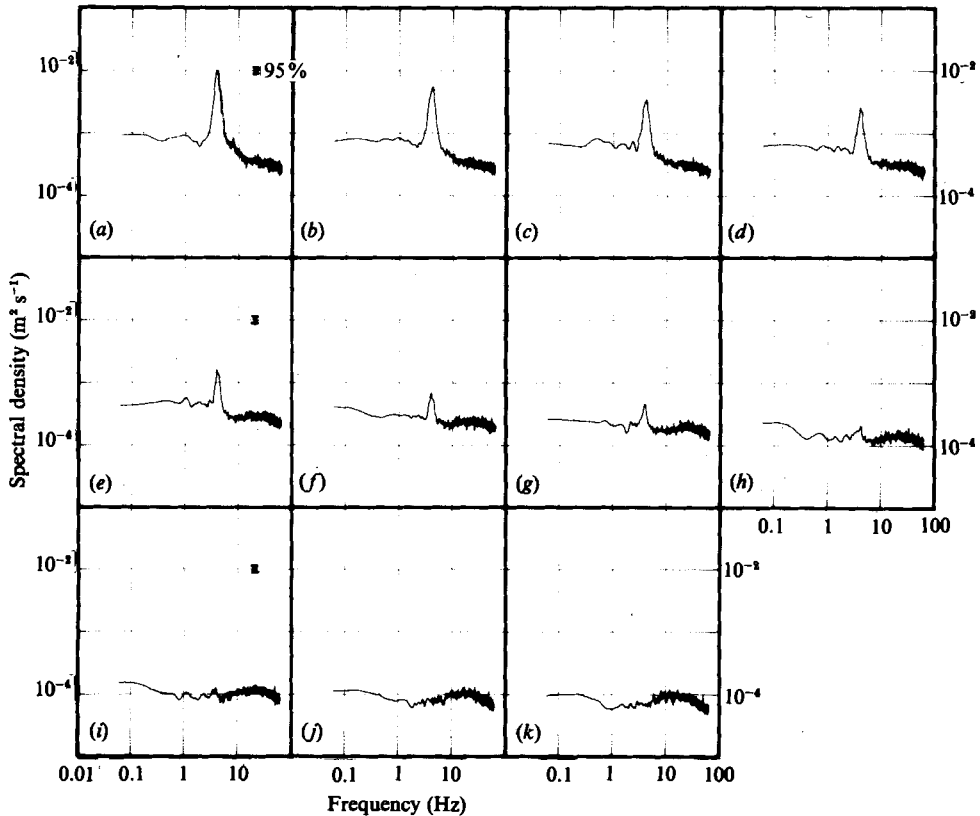
FIGURE 5. Power spectra of w. Heights are the same as in figure 4.

does not change except for that around the wind-wave peak frequency, and in the upper layer $(e-k)$ the spectral density decreases over the whole frequency range with increasing height. The increase of the spectral density at the wave peak with decreasing height corresponds to the small increments of turbulence intensity seen in figure 3. The cross-spectral analysis by KOKT indicates that the wind-wave peak components of the velocity fluctuations are not important for the Reynolds-stress production because of the phase difference of $90°$ between u and w. Therefore, in the logarithmic boundary layer, all of the momentum flux is caused by the turbulence fluctuations (except the wave peak components) which can be thought to have a constant intensity.

Power spectra of u and w calculated to investigate the high-frequency range (not shown here) have a $-5/3$ slope at every height for frequencies higher than about 100 Hz.

4. Ordered motion in the outer boundary layer

4.1. *Visualization of ordered motion using paraffin mist*

Liquid paraffin mist was used to visualize large-scale motions in the turbulent boundary layer. The mist generator is illustrated in figure 6. We observed how the mist spread as it was continuously released from a point source placed near the water surface in the centre between the two sidewalls of the tunnel. The mist generator is
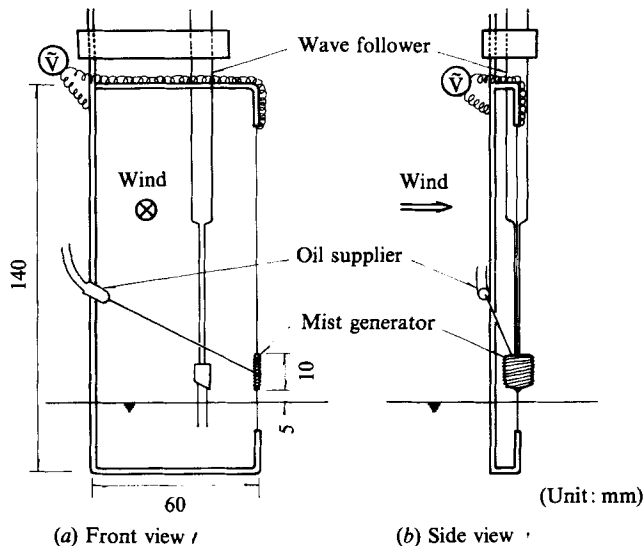
FIGURE 6. Mist generator mounted on the wave follower.

asbestos to which liquid paraffin was continuously supplied through an injection needle and heated with a nichrome wire. The distance between the lower end of the asbestos and the fluctuating water surface was maintained at about 0.5 cm by the wave follower, which means that the mist source was always located in the under part of the logarithmic boundary layer ($z < 3$ cm in this case, see figure 9).

The mist was photographed by a high-speed streak camera at a fetch 1 m downstream from the mist source. As a light source, we used a specially designed power stroboscope, PS-333S manufactured by Sugawara Laboratories Inc. The stroboscope placed on the top of the tunnel beams a sheet of nearly parallel light through a slit with a variable width (0–20 mm) and a length of 400 mm. It slices the mist pattern in the air flow optically and makes the configurations of the mist boundary visible. The slit was set at a 5 mm width throughout this experiment. Three xenon gas lamps, which flash in turn, were mounted in series in the lamp house in order to realize flash rates up to 150 Hz. The areas illuminated by each of the three lamps are slightly different; this is exemplified in figure 10 (a) where pictures 1, 2 and 3 have illuminated mist (white) areas slightly different from each other. However, the common area just under the slit (about 50 cm long at the water surface) was always included. The photographed area in the plane along the vertical centreline of the tunnel was about 20 cm high and 80 cm long.

Typical results of visualization with the paraffin mist are shown in figure 7, indicating large-scale motions in the outer boundary layer. The photographs in figure 7 were taken at fetch = 3.8 m. The dark undulations at the bottom show the profiles of wind waves. The fluid, which was marked with the mist in the vicinity of the water surface, reaches the outer part of the boundary layer, forming a train of characteristic shapes at the edges, hereafter called 'bulges'. This observation proves that active diffusion is occurring in the air flow from near the water surface to the outer boundary layer. As seen in the pictures, the slight bending forward of the bulges is similar to the ordered motions visualized with smoke in the turbulent boundary layer over a plane surface (for example, see Falco 1977). However, it should be noticed that the bulges have a horizontal lengthscale corresponding to the wavelength of the wind

Wind ⟶
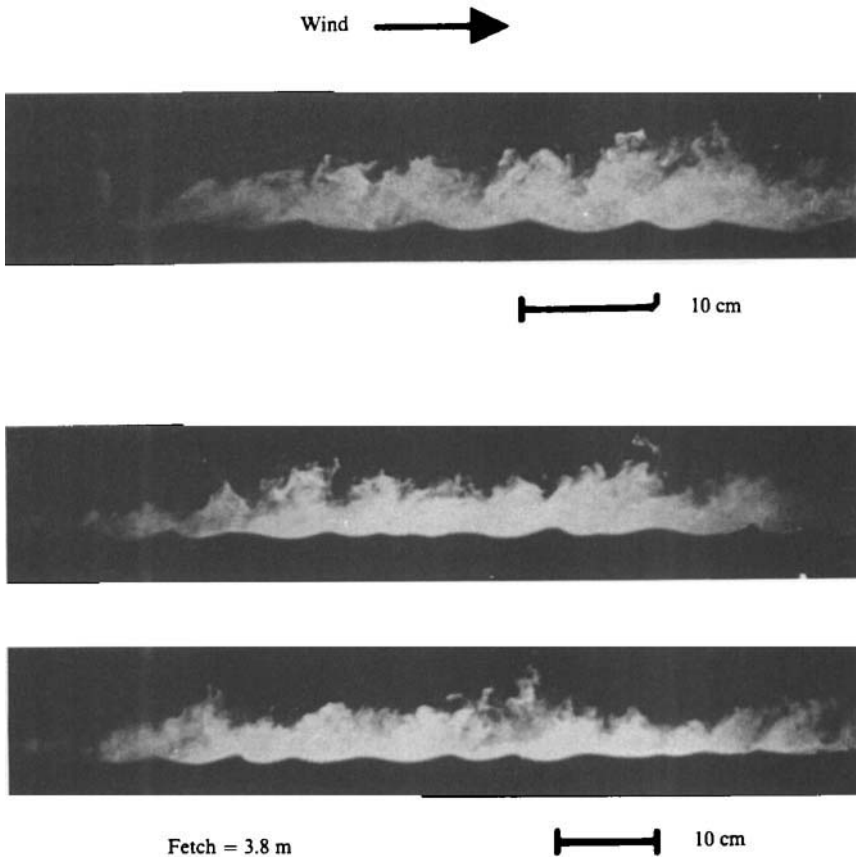

Fetch = 3.8 m   10 cm

FIGURE 7. Visualization of large-scale ordered motions over wind waves by paraffin mist.

waves. Each of these bulges represents the large-scale ordered motion in the boundary layer over wind waves, as will be confirmed in the following section by the combination of the hot-wire measurements and mist photographs.

4.2. *Visualization of ordered motion combined with hot-wire measurements*

For further understanding of the ordered motion captured by the mist photographs in the previous section, we conducted experiments in which successive pictures of the mist were taken, combined with simultaneous velocity measurements by the hot wire; that is, a Lagrangian observation of the large-scale motions with successive pictures was combined with a concurrent Eulerian measurement by the hot wire.

Figure 8 shows the arrangement of the instruments. Four single-wire wave gauges were hung from the top wall of the tunnel; the right-hand wave gauge was placed at the fetch of the hot wire. The wave gauges were placed about 1 cm behind the illuminated plane, and their faint images in the pictures were used to determine the locations of the bulges. Signals indicating the stroboscope flashes were recorded on the tape recorder together with the outputs of the hot wire and the wave gauges. The experiments were done at wind speed U_1 with the hot wire at heights of $z = 5$ and 7 cm, and for U_2 at $z = 4$ cm.

Since hot-wire anemometer is sensitive to the surrounding air temperature, measurements in the air flow with and without the paraffin mist were made at seven

Glass wall of wind-wave tunnel

(a) Top view   ▭ Streak camera
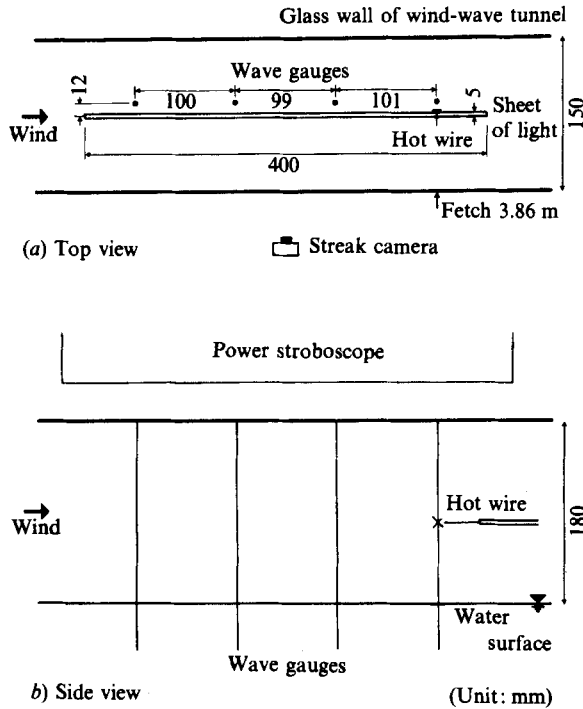

b) Side view   (Unit: mm)

FIGURE 8. Arrangement of the instruments used for the visualization experiment combined with the hot-wire measurements.
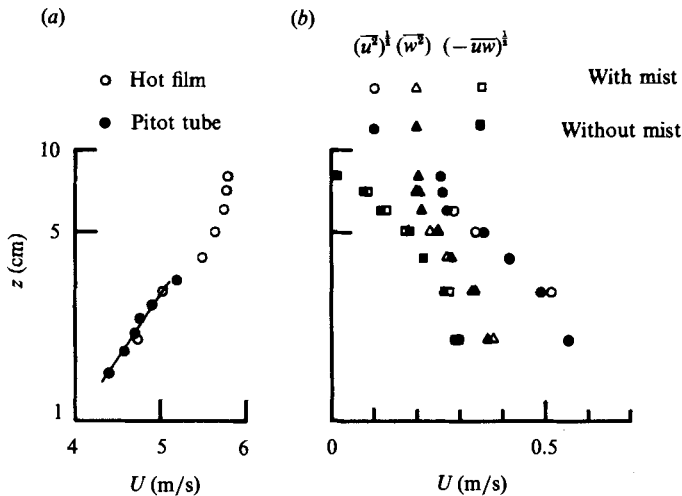

FIGURE 9. Examination of validity of the hot-wire measurements in the air flow with the mist. (a) The profile of the mean flow and (b) the profiles of $(\overline{u^2})^{\frac{1}{2}}$, $(\overline{w^2})^{\frac{1}{2}}$ and $(\overline{-uw})^{\frac{1}{2}}$ (see the text).

heights ($z = 2$, 3, 4, 5, 6, 7 and 8 cm) at U_1 in order to examine the validity of using the hot wire for this experiment. Figures 9(a) and 9(b) show vertical profiles of the mean air velocity and the statistical values of the velocity fluctuation, respectively. The mean velocity in the mist flow was slightly lower than that in the flow without the mist at every height owing to a slight increase in temperature

caused by the mist generation; but the differences were 0.02–0.07 m/s which is about 1 % of the mean flow. Since the differences are not distinguishable in figure 9(a), only the values obtained under no mist are plotted. The mean velocity near the water surface determined by the Pitot-static tube is also plotted in the figure, which confirms the logarithmic profile in the lower layer and the wake profile in the upper layer. The statistical values $(\overline{u^2})^{\frac{1}{2}}$, $(\overline{w^2})^{\frac{1}{2}}$ and $(\overline{-uw})^{\frac{1}{2}}$ measured under both conditions (figure 9(b) show that the differences between the two are small and not systematic. Therefore, these differences may be attributed to errors due to insufficient data length (20 s). These profiles indicate the features of the turbulent boundary layer described in §3. We conclude from these results that the influence of the mist on the hot-wire measurements is almost negligible.

A sequence of pictures numbered 1–24 is shown in figure 10(a) and the simultaneously obtained records of the velocity and wind waves in figure 10(b). The time interval between successive pictures was 6.7 ms. The wind at speed U_1 (5.75 m/s in the core of the tunnel) is blowing from the left. A horizontal rod carrying the hot wire at its upstream end (fetch = 3.8 m) is seen on the right of the photographs. The hot wire was placed at $z = 7$ cm which is approximately the outer edge of the turbulent boundary layer. The mist generator was at fetch = 2.8 m (about 10 cm to the left out of the view). Figure 10(b) shows, from the top, the time series of $u(t)$, $w(t)$, the instantaneous Reynolds stress $u(t)w(t)$, the surface displacement and the stroboscope signals, the numbers on which indicate the times when the pictures of the same number were taken.

The bulges, which have a lengthscale equal to the wavelength of the underlying wind waves, are seen in the pictures, moving from left to right. The lines designated a–d show the movement of the bulges which reach the hot wire up to No. 24. The white arrows a–d in the pictures show the bulges meeting the hot wire during this sequence. The line W is added to show the propagation of a wind wave. Since the inclination of the lines indicates the travel speed, the phase speed of wind waves is much slower than the travel speed of the bulges. It is evident from figure 10(b) that the characteristic variations in the velocity signals are related to the passage of the bulges through the hot wire. The times when the bulges met the hot wires, taken from the photographs, are shown in figure 10(b) by the same symbols a–d as in figure 10(a). When the bulges reach the hot wire, a low velocity ($u(t) < 0$) appears, usually coupled with an upward velocity ($w(t) > 0$) and, as a result, large negative values of $u(t)w(t)$ are produced at $z = 7$ cm.

The bulges can be followed as they pass through the photographed area. This means that the distance of persistence of the bulges is longer than 50 cm. As bulges travel they evolve in two different ways. First, the remarkable growth of the bulge d can be seen in the pictures of figure 10. This evolution of the bulge's configuration and location, derived from the pictures, is sketched in figure 11(a). The bulge d first appears in picture 9 and reaches the hot wire in pictures 22 and 23. At first it is about 4 cm in height and eventually becomes about 8 cm. The characteristic velocity of its edge was obtained from figure 11(a); the streamwise speed is 5.10 m/s ($0.89U_\infty$), and the upward speed 0.45 m/s. These values correspond well to the values of the velocity signals specified by d in figure 10(b).

Another example showing the remarkable growth of the bulge from about 3 cm to 8 cm in height was found in the other sequence of pictures and is illustrated in figure 11(b). The streamwise speed of the movement is 5.13 m/s ($0.89U_\infty$) and the upward speed is 0.52 m/s. It is noticeable from figure 11(a), (b) that the bulges always have a horizontal lengthscale of one wavelength of the underlying wind waves.
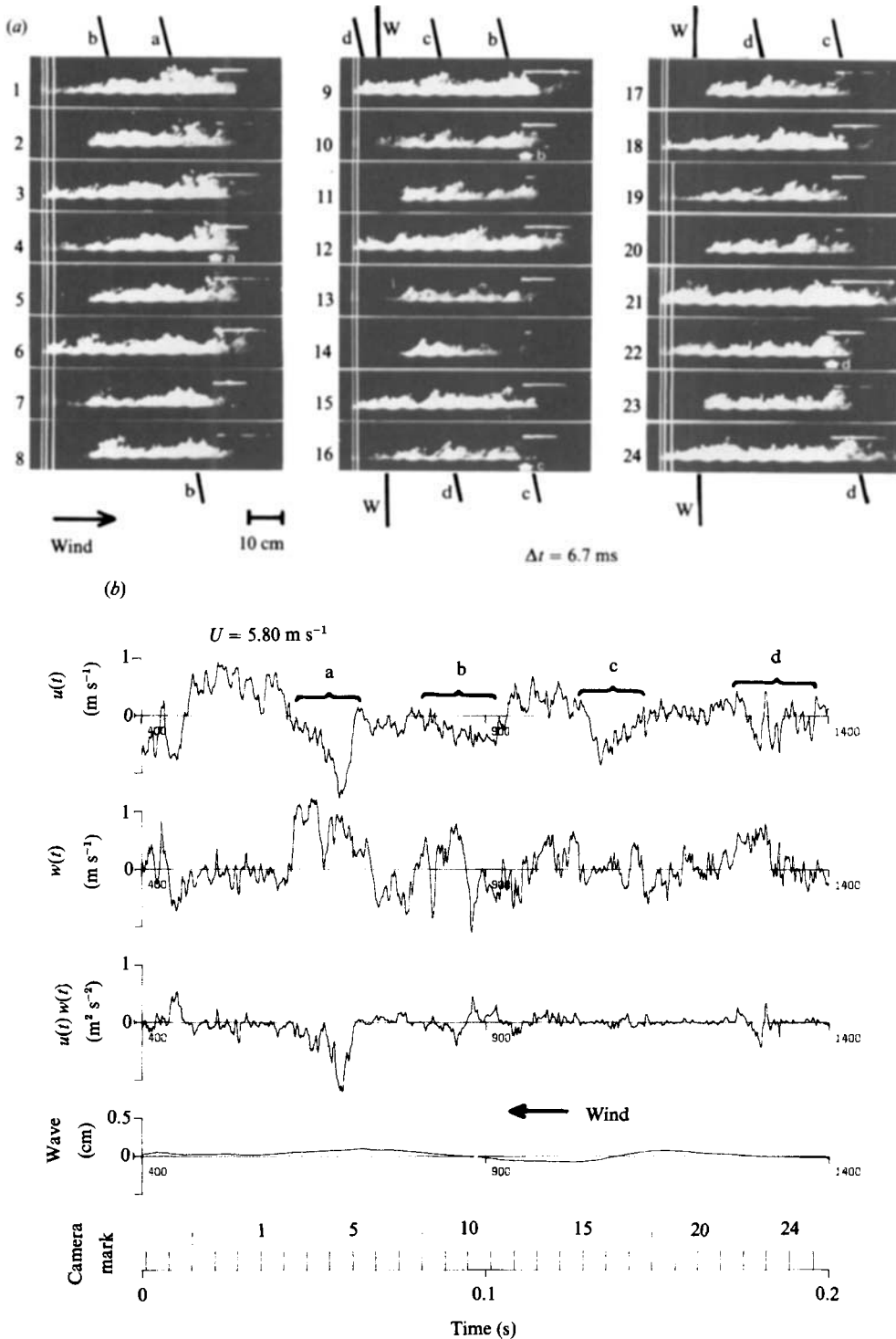
FIGURE 10. Results of the visualization combined with the hot-wire measurements at U_1. A sequence of pictures of the visualization of ordered motions by paraffin mist. (*b*) Records of the hot wire at $z = 7$ cm and the wave gauge at the same fetch as the hot wire, simultaneously obtained with the pictures of (*a*). The bottom figure shows the stroboscope signals, where numbers correspond to the times when the pictures of (*a*) were taken (see the text).
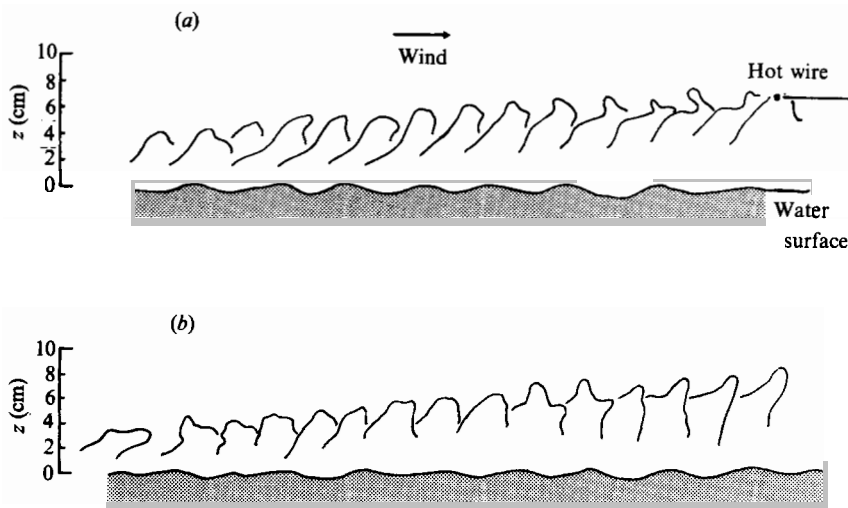
FIGURE 11. Sketch illustrating the evolution of bulges, which show a remarkable growth
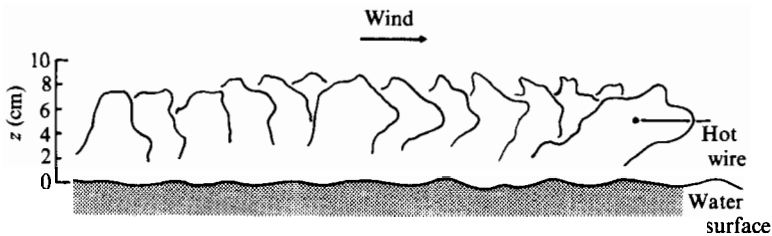in height.

FIGURE 12. Showing the evolution of a bulge, which we call an FD ordered motion
(see the text).

It can be inferred from these results that an air mass originating from the lower part of the logarithmic boundary layer ($z < 3$ cm in this case) forms the ordered motions seen in the outer boundary layer, without losing its identity, while it grows remarkably in height. Thus, one of the mechanisms transferring the air marked with mist near the water surface is this evolution of the bulge. This mechanism will be discussed later when considering the experimental results of §§5 and 6.

The second type of bulge evolution is one in which the bulge does not change its height significantly, but is transformed while moving ahead. Bulges a and c of figure 10 (a) are examples of this, and a typical case is shown in figure 12 where the hot wire was at $z = 5$ cm. Although the bulge bends forward at the hot-wire position, it maintains the horizontal lengthscale of the wavelength of the wind waves. We consider that this type of bulge evolution may be the stage following the remarkable growth in height described above. Hereafter, we call this type of bulge the fully developed (FD) ordered motion or simply the FD.

The velocity fluctuation associated with the passage of the FD was obtained by conditional sampling of the velocity signals. First we looked at the successive pictures carefully and found an FD ordered motion. Since we were able to recognize the FD passing through the hot wire from three or four pictures, the position of the hot wire relative to the bulge could be determined to obtain the velocity distribution
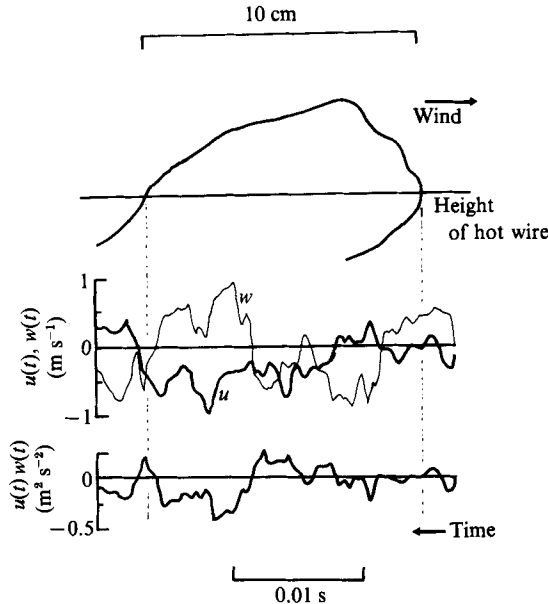
FIGURE 13. An example of the conditional sampling of the velocity fluctuations and instantaneous Reynolds stress inside the bulge, shown in figure 12. The hot wire was placed at $z = 5$ cm.

inside the bulge. As an example of this kind of sampling, in figure 13 are shown the velocity fluctuations and the instantaneous Reynolds stress caused by the FD of figure 12. In the windward side of the bulge, substantial Reynolds stress is generated by the moving upward of low-speed air. By contrast, high-speed air moves downward to its leeward side.

Ten FD ordered motions with the corresponding velocity fluctuations were sampled. Velocity signals inside the collected FDs were averaged: the mean streamwise velocity is 5.33 m/s $(0.93U_\infty)$, the mean upward velocity is 0.06 m/s and the Reynolds stress is -0.09 m^2 s^{-2}. It is noted that the speed of the FD ordered motion is slightly higher than that of the rapidly growing bulge $(0.89U_\infty)$. Since the local Reynolds stress at this height is -0.04 m^2 s^{-2}, it is evident that the FD ordered motions produce a major part of the Reynolds stress at $z = 5$ cm.

Positions inside each FD were normalized by its horizontal length at $z = 5$ cm to obtain ensemble-averaged characteristics of the FDs as shown in figure 14. The velocity vectors shown in the top figure are referenced to an observer who moves at the mean speed of the bulge, 5.33 m/s. We find a large-scale motion slowly rotating around the core of the bulge. Considerable activity is noticeable on the rear part of the bulge; it is caused by a low horizontal velocity coupled with an upward velocity. Entrainment of the high-speed air from the upper layer occurs at the streamwise interface. These results indicate the existence of mutual interaction between the FD ordered motion in the outer boundary layer and flow in the inner layer. This structure of the FD ordered motion is quite similar to the common physical concept of the ordered motion over flat plates (Cantwell 1981), associated with the activity of a burst of low-speed fluid from a streaky structure near the wall which systematically produces a large part of the Reynolds stress. In order to obtain a full picture of the physical concept of ordered motion over wind waves, the flow structure in the inner layer will be examined in the following sections.
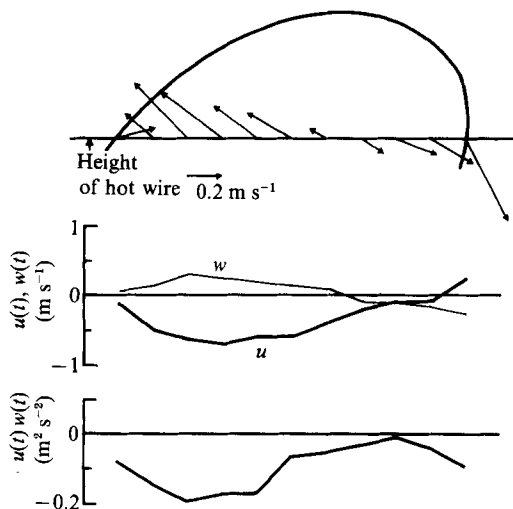
FIGURE 14. Ensemble-averaged velocity fluctuations and instantaneous Reynolds stress inside the fully developed ordered motion. In the top figure are shown velocity vectors with reference to an observer moving at the mean speed of the bulges.

The result of the experiment carried out at U_2 ($U_\infty = 8.32$ m/s) and the hot wire at $z = 4$ cm is shown in figure 15 in the same way as figure 10. Since this wind was stronger than that of the previous case, larger wind waves were generated at the same fetch. It can be seen that the bulges have a horizontal lengthscale equal to the wavelength of the wind waves underlying them. As can be seen in the time series (figure 15b), the passage of the bulge through the hot wire corresponds to the characteristic velocity fluctuations of low horizontal velocity which produce substantial Reynolds stress by coupling with the upward velocity. When we compare this result with that of the previous wind condition, it is obvious that, although the ordered motions also exist in this case, the amplitude of the associated velocity fluctuations is larger, and their passage is more frequent since the speed of the ordered motion is faster. It will be shown in §6 that the bursting phenomena observed in the inner layer are a major mechanism in Reynolds stress production, and it is suggested that the ordered motions work systematically together with the bursting phenomena to maintain the turbulence in the whole turbulent boundary layer and a constant momentum flux in the logarithmic boundary layer. A comparison of the results for these two different wind conditions suggests that an increase of Reynolds stress with wind speed (see table 2) might be explained by the increase in the amplitude and the number of the ordered motions.

Lastly, in order to show the horizontal lengthscale of the ordered motion more objectively, wavenumber spectra of the profiles of both the mist edge and the water surface were calculated. Figure 16 shows the profiles traced from the top photograph of figure 7. The profiles were digitized, and then some parts of the bulge profiles were modified as shown by the dashed line in figure 16 to obtain a single-valued function of the profile for x. The horizontal length of the traced area was 350 mm and the digitizing interval was 1 mm. The traced data include about six wind waves at U_1 and about three at U_2.

The maximum entropy method (MEM) was employed to obtain the wavenumber spectra since the data lengths were not long enough to calculate reliable spectra

(b)

Wind   10 cm

$U = 8.03 \text{ m s}^{-1}$
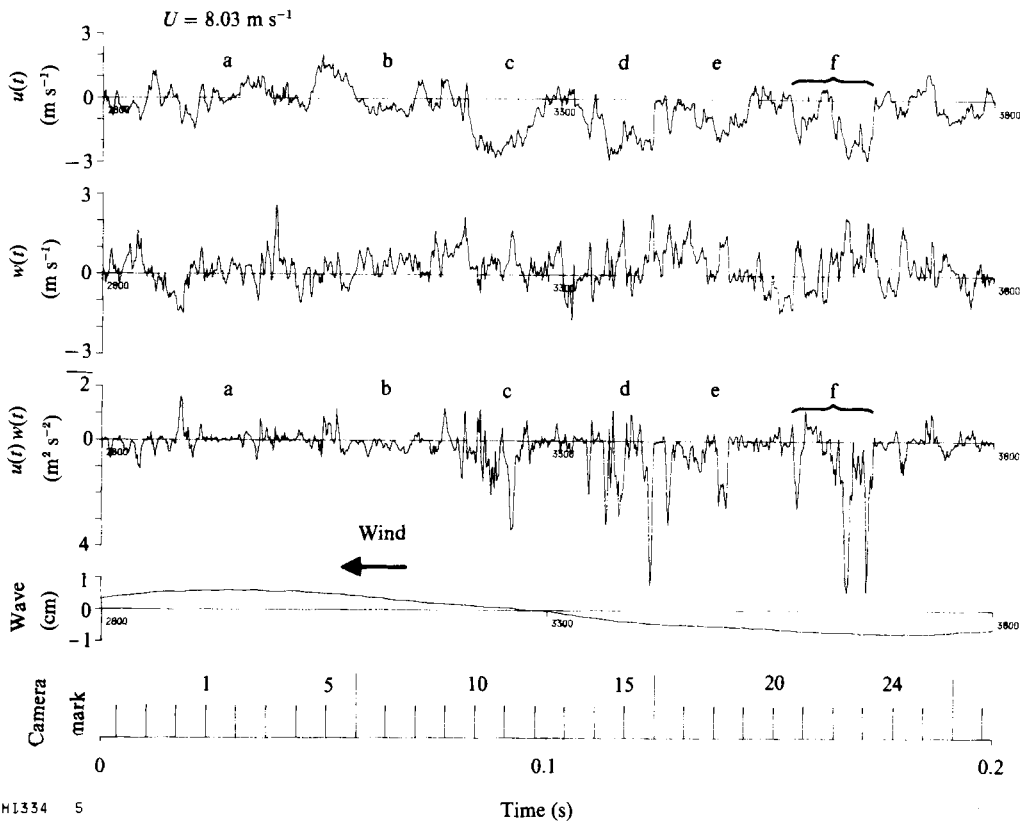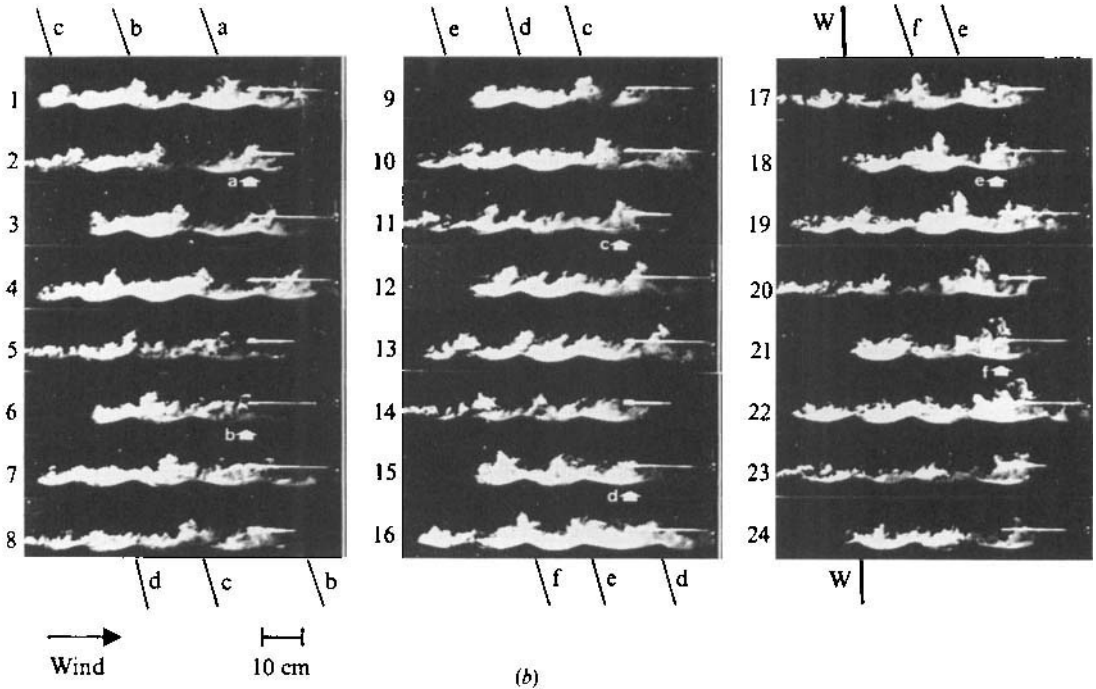
FIGURE 15. Same as figure 10, except at U_2 and with the height of the hot wire $z = 4$ cm.

FIGURE 16. Profiles of the bulges and wind waves traced from the top photograph of figure 7 (see the text).
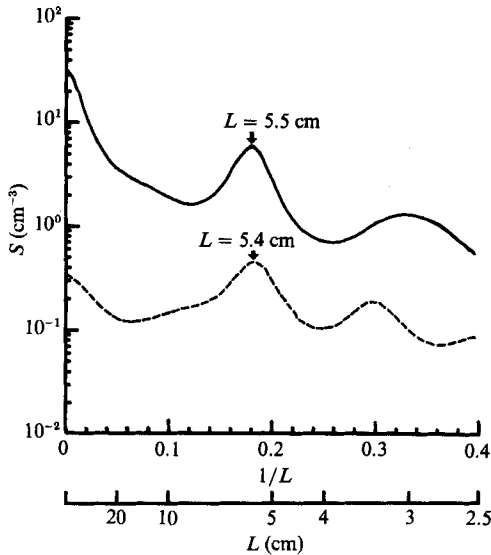

FIGURE 17. MEM spectra of the bulge and the wind-wave profiles shown in figure 16. The solid line shows the bulge spectrum and the dashed line the wind-wave spectrum.

by other methods. Burg's algorithm was used to calculate the MEM spectra for 80 prediction-error coefficients. Figure 17 shows the MEM spectra of the profiles of figure 16. The spectral peak of the water-surface profile at length $L = 5.4$ cm indicates the main wind waves, and the corresponding peak of the bulge spectrum is seen at $L = 5.5$ cm. The 50 photographs of the visualization at U_1, including those of figures 7 and 10, were traced and analysed using MEM. Since the photographs in this case show five or six wind waves developing with fetch, the waves seen on the left side of the photographs are usually shorter than the waves on the right. Therefore the spectral peaks of wind waves appeared in the range of $L \sim 4.5$–7.5 cm. Figure 18 shows the averaged spectra of the 50 samples. A wind-wave peak is seen at $L = 6.2$ cm. The 36 bulge spectra among the 50 samples have shown significant peaks within the range of $L = 6.2 \pm 1$ cm, and the average of the 50 spectra in figure 18 shows a peak at $L = 7.0$ cm. Fairly good agreement between the horizontal scales of the bulge and the wind waves is confirmed.

The data at U_2 were analysed similarly (including the data of figure 15) and the result corresponding to figure 18 is shown in figure 19. Since only two or three wind waves were pictured in this case where there is little growth of waves, the averaged
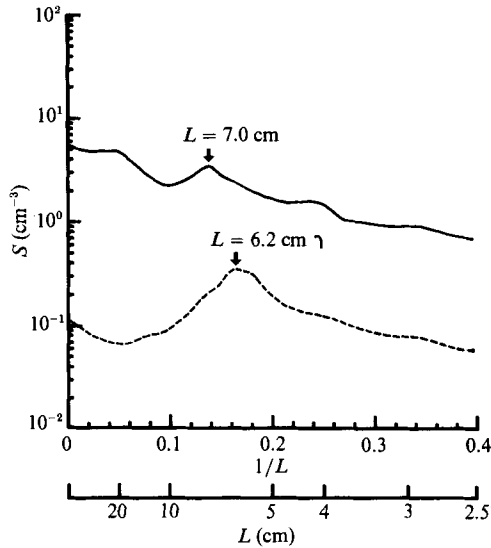
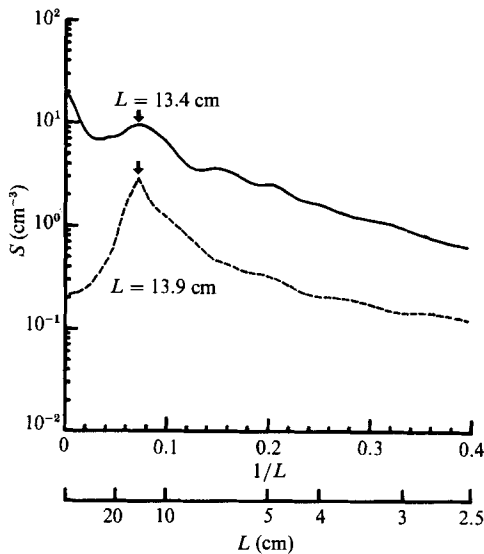FIGURE 18. The averaged MEM spectra of the bulge (solid line) and wind waves (dashed line) at U_1.

FIGURE 19. The averaged MEM spectra of the bulge (solid line) and wind waves (dashed line) at U_2.

spectrum of wind waves shows a sharper peak than the previous case. The peak wavelength ($L = 13.4$ cm) of the bulge agrees with that of the wind waves ($L = 13.9$ cm).

5. Air-flow separation over wind waves

5.1. *Instantaneous velocity-shear measurements using two hot wires*

In order to measure air velocity fluctuations near the water surface, especially below the wind-wave crest level, we used a wave follower which maintained measuring
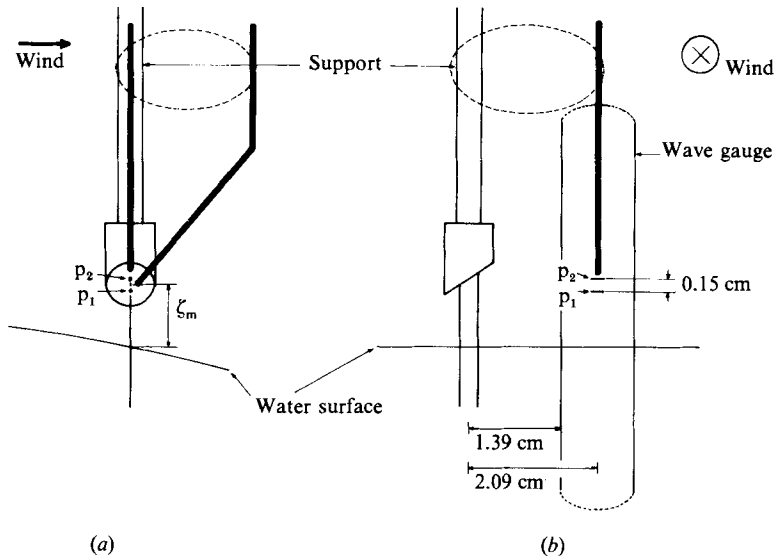
FIGURE 20. Instruments for measurements of the instantaneous velocity shear in the air flow near the water surface: arrangement of hot wires, a capacitance-type wave gauge and the support of the wave follower: (*a*) side view and (*b*) front view.

probes (hot wires in the present experiment) at a constant height from the fluctuating water surface. The wave follower consists of a servomotor and a support with two platinum electrodes at its lower end. The probes are mounted on the support. The servomotor moves the support to keep a constant distance between the probes and the fluctuating water surface by monitoring the resistance between the two partly immersed electrodes. The movement of the support, showing the relative positions of the hot wires, is output as a variation in voltage.

A capacitance-type wave gauge was used to determine the precise distance between the hot wires mounted on the support and the fluctuating water surface just under them. The use of the wave gauge in addition to the wave follower was required for the following two reasons. The hot wires were set with the support at the same fetch but 2.09 cm apart in the y-direction to avoid the influence of the support on the wind field (figure 20 a, b). Since the wind waves are not completely two-dimensional, the elevation of the water surface at the position of the electrodes sometimes differs from that just under the hot wires. Secondly, the wave follower could not perfectly follow wind waves with a sharp gradient at the forward face of their crests as seen in figure 1(b, c). The hot wires were set between the two enamel-coated lines of the wave gauges (figure 20b). The degree of tracking of the wave follower can be seen in figure 21, which proves that our primary aim of measuring the air velocity below the crest level was achieved. There were no electric mutual interactions between the wave gauge and the wave follower.

The two hot wires arranged in parallel and 0.15 cm ($= \Delta z$) apart in the z-direction were used to detect velocity and velocity-shear fluctuations near the water surface (figures 20a, b). The lower and the upper hot wires are called p_1 and p_2, and the absolute values of the velocity vectors measured by p_1 and p_2 are designated q_1 and q_2, respectively. The distance from the water surface at rest to the middle of the two hot wires is defined as ζ_m. The relative positions of the devices and the water surface at rest were obtained photographically. Because of the special characteristics of the
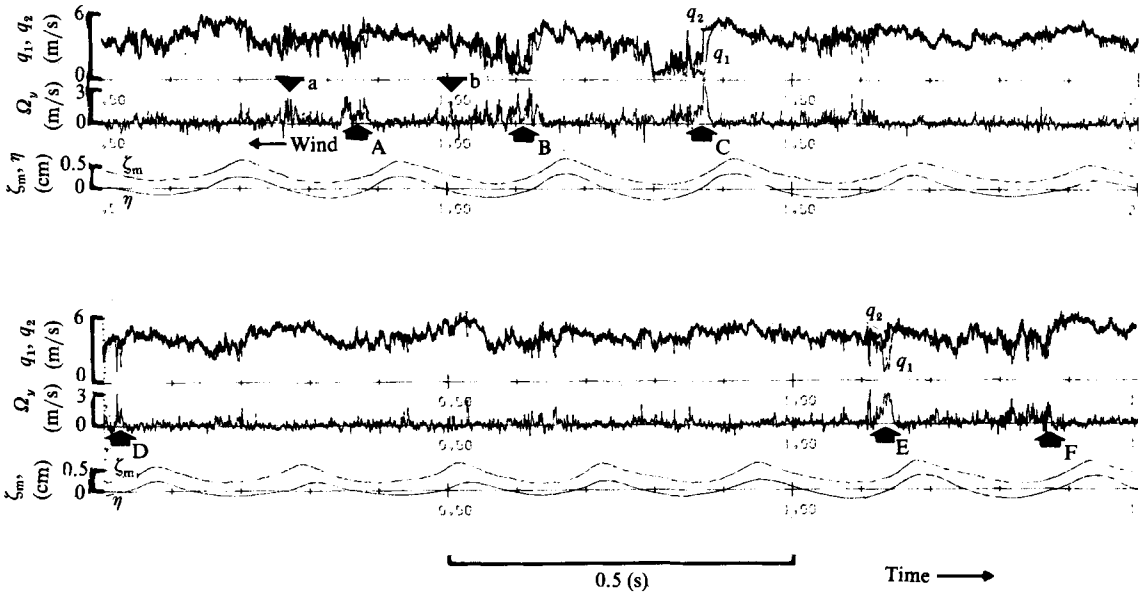
FIGURE 21. Time series of q_1, q_2 and $\Omega_y (= q_2 - q_1)$ together with the water surface displacement η and the height of the two hot wires ζ_m. Arrows A–F indicate conspicuous peaks of Ω_y over the leeward side of wind waves, and arrows a and b over the windward side.

wave-following system used here, the minimum value of ζ_m we could achieve was 0.69 cm. Throughout this experiment, ζ_m was set at the minimum.

The purpose of this arrangement of the hot wires is to detect a high-shear region, which is formed in the vicinity of the water surface. We define the instantaneous velocity shear as the difference between q_1 and q_2, that is,

$$\Omega_y(t) = q_2(t) - q_1(t).$$

The vorticity is $\Omega_y(t)/\Delta z$ for the time when both of the velocity vectors point downwind, such as in a separated shear flow just behind the separating point.

5.2. *Detection of air-flow separation behind a wind wave crest*

Figure 21 shows a sequence of simultaneous records: the positions of the hot wires $\zeta_m(t)$, the surface displacement $\eta(t)$, the velocities $q_1(t), q_2(t)$ and the velocity shear $\Omega_y(t)$. It is evident from the figure that, over the troughs of wind waves, except for a few small ones, the two hot wires are located at positions lower than the crest level. Over some wind-wave troughs, characteristic variations appear in $q_1(t), q_2(t)$ and $\Omega_y(t)$, simultaneously. Conspicuous peaks of $\Omega_y(t)$ (marked by arrows A–F in figure 21) showing large positive values are observed, and at the same time $q_1(t)$ and $q_2(t)$ also show drastic changes. A typical example of a record demonstrating these characteristic variations over a trough is shown in figure 22.

Noticeable features of these variations are: (1) conspicuous peaks of $\Omega_y(t)$ with large amplitude appear at leeward positions close to the crests of wind waves; (2) just before the time they appear, $q_1(t)$ and $q_2(t)$ show very low velocities, sometimes nearly zero; (3) abrupt increases in $q_1(t)$ and $q_2(t)$ follow the very low values, and a short time interval between these increases causes the conspicuous peak of $\Omega_y(t)$; and (4) positive peaks of $\Omega_y(t)$, which are not so large, sometimes appear over the windward side of wind waves (as marked by arrows a and b in figure 21) when the peaks over
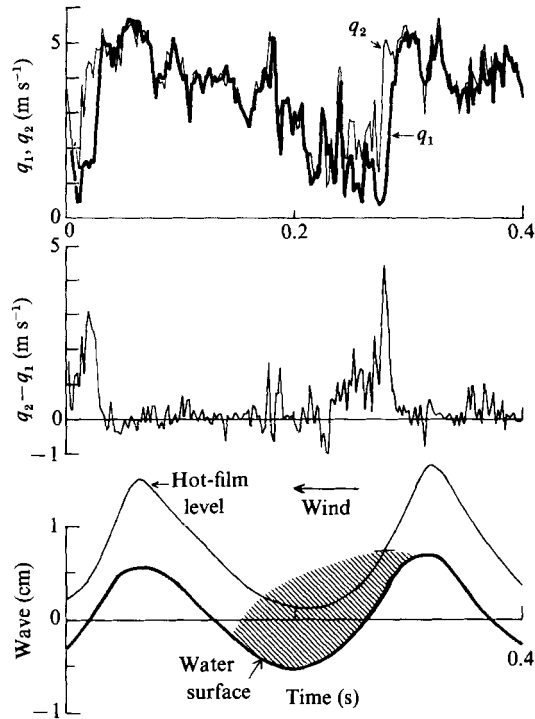
FIGURE 22. A typical example of the time series showing conspicuous peaks of Ω_y. An expected separation bubble is illustrated shaded in the bottom figure.

the leeward side are observed. These characteristic variations can be explained by the existence of a separation bubble behind the wind-wave crest. The expected separation bubble is illustrated at the bottom of figure 22. The conspicuous peaks over both the leeward and windward sides of the crest indicate detection of the high-shear layer caused by the separated shear flow.

As seen in figure 21, there exists another pattern of velocity signals which does not show the drastic change over wind waves. This pattern corresponds to the air flow along the undulating water surface. As previously revealed by Kawai (1981, 1982), two distinct air-flow patterns (with and without separation) exist each with significant frequency.

To determine the position of the high-shear layer, the signals over wind-wave troughs were sampled using the following criteria: (1) the peak value of $\Omega_y(t) > 2.5$ m/s, with the lowest value of $q_1(t) < 1.0$ m/s; (2) for peaks over the windward side, peak values of $\Omega_y(t) > 1.5$ m/s followd by the peak of condition (1) over the leeward side of the next wave. These conditions were carefully established to sample these signals showing the typical separation phenomena according to the concept of the detection described above. From the signals of figure 21, for example, only three troughs with the vorticity peaks Bb, C and E were selected, but the others with Aa, D and F, which did not meet the criteria, were rejected even though they appeared to have the characteristics of the separation phenomenon.

Among 876 wave troughs, 40 troughs with 40 peaks over the leeward side and 11 over the windward side were sampled. The mean values of the peaks are 2.83 m/s (with maximum 4.42 m/s) over the leeward side and 1.93 m/s (2.36 m/s) over the
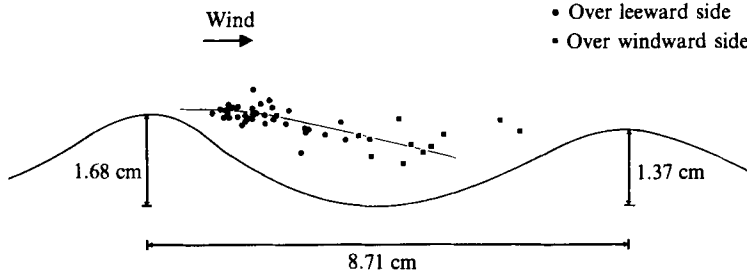
FIGURE 23. Detection of the high-shear layer at the outer edge of the separation bubble.

windward side. The positions of the high-shear layers (x, z) were normalized: x was converted to phase using the wavelength, and z was normalized with the wave height of the windward wave. Figure 23 indicates the normalized position and the outer edge of the expected separation bubbles. The value of the wavelength, which was calculated from the period by applying the dispersion relation of gravity waves in deep water, and the value of the wave height in the figure indicates the average of the 40 samples. The average height $H = 1.68$ cm of wind waves which cause the separation is considerably larger than the significant wave height $H_{\frac{1}{3}}$ of 1.07 cm, but on the other hand, the average wavelength λ of 8.71 cm is shorter than the wavelength derived from the significant wind-wave period, 9.74 cm. This means that the surface slope of wind waves that cause air-flow separation, $H/\lambda = 0.19$, is much greater than that of the significant wave, $H/\lambda = 0.11$.

The positions of the high-shear layer over the leeward side concentrate at the same level as the crest (figure 23). Some of them are higher than the crest. The expected edge of the separation bubble near the wave crest is very similar to Kawai's result (Kawai 1982, figure 13) on the pattern at the beginning of separation. This fact supports Kawai's (1982) suggestion that separation occurs at a sharp wave crest, not at a stagnation point which had been expected on the leeward face of the wave (Banner & Melville 1976; Okuda 1982*b*). Kawai (1982) did not explain the reason for the air-flow separation explicitly, but all of his results strongly suggested that 'the dynamical reason is the well known one: the onset of separation depends on the interplay between the adverse pressure gradient on the downwind side of a wave, and the turbulence in the air flow (Csanady 1985)'. The separating streamline comes down gently from the crest level until it reattaches on the windward side of the preceding wave. Kawai's figure 13 shows an upward streamline after separation, which corresponds to some points higher than the crest level in figure 23. However, as a representative pattern of the separated streamline, Kawai's figure 13 should be replaced by figure 23.

On the other hand, the positions of the high-shear region over the windward side of the preceding wave are scattered, which coincides with the observation of Kawai (1982). He has pointed out that 'this variety (of the flow structure or of the positions of the vorticity peaks) seems to be related to an instability of the high shear layer accompanied by separation'. The structure of this air-flow separation, including reattachment of the separated shear flow, is similar to that behind a 'backfacing' step. When the separated shear flow is at about the same level as the wave crest, it will be possible to deal with this flow as a free boundary layer. Therefore, we can examine the linear stability theory of free boundary layers, though we cannot directly apply the results of the theory because our case concerns turbulent air flow.
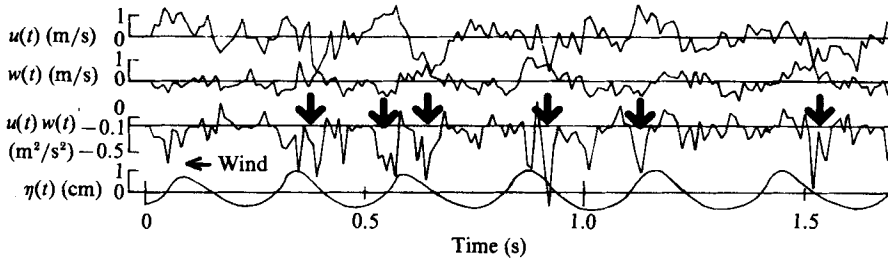
FIGURE 24. Detection of the bursting phenomena over wind waves. Velocity fluctuations were obtained at $z = 1.62$ cm at fetch $= 6$ m at U_1 (taken from Kawmura *et al.* 1981).

The mean value of the velocity difference across the high-shear region over the leeward side, 283 cm/s, was detected by two hot wires with a 0.15 cm interval. When we assume a parallel shear flow of the free boundary layer, the lengthscale of $l \sim 0.15$ cm, the velocity scale $U \sim 140$ cm/s ($2U = 283$ cm/s) and the kinematic viscosity $\nu = 0.15$ cm^2/s give a Reynolds number $R = lU/\nu = 140$. Since the free boundary layer is very unstable when considered from the point of view of linear stability theory, we can expect much turbulence generation in the shear flow from that value of $R = 140$ (Lessen 1950; Tatsumi & Gotoh 1960). The air flow over the wind waves originally contains large disturbances of the turbulence which may be suitable for turbulence generation in the separated shear layer. The scattered positions of the vorticity peaks over the windward side and the observation of the separated shear layer by flow visualization (Kawai 1982) can be considered to be due to turbulent motions which are generated in the separated shear flow and develop with distance from the separating point.

6. Bursting phenomena over wind waves

6.1. *Brief introduction and experiment*

For the air flow over wind waves, KOKT has identified phenomena similar to the bursting phenomena over flat plates. KOKT measured velocity components ($U + u(t)$, $w(t)$) using an X hot wire at fixed positions near the water surface in the same wind-wave tunnel as this study. The time series, in which the bursting phenomena were detected, is given in figure 24 taken from KOKT. Large negative spikes marked by arrows in the signal of $u(t) w(t)$ (called the instantaneous Reynolds stress) are characteristic of these phenomena. The noticeable features of the spikes are summarized as follows: (1) the spikes usually appear at positions close to the crest of wind waves with relatively large wave height; (2) the frequency of occurrence of the spikes on the windward side is greater than that over the leeward side and the amplitude of the spikes is greater on the windward side; and (3) the spikes over the windward side are always formed by the coupling of negative $u(t)$ and positive $w(t)$ (like the burst over flat plates). Over the other side, formation is mostly by the coupling of positive $u(t)$ with negative $w(t)$ (like the sweep). These phenomena make a significant contribution to Reynolds-stress production. Hereafter, we call these 'bursting phenomena' over wind waves; according to the definitions adopted in the turbulence literature, the ascending low-speed air mass is called a 'burst' and the descending high-speed air mass a 'sweep'.

In order to study the bursting phenomena in relation to the ordered motion investigated in the outer boundary layer and the separation bubble in the vicinity of

Height of hot wire (cm)	C (m^2/s^2)	τ_d (s)	Number of wind waves	N_b	Burst	
					T_b as a percentage of T	uw_b as a percentage of uw
1.2	0.88	0.026	1284	1987	17%	40%
1.4	0.90	0.026	1318	1757	15%	35%
1.6	0.90	0.026	1331	1639	14%	32%
1.8	0.85	0.026	1381	1798	15%	33%
2.0	0.85	0.026	1356	1843	16%	33%

Height of hot wire (cm)	N_s	Sweep	
		T_s as a percentage of T	uw_s as a percentage of uw
1.2	1586	13%	33%
1.4	1368	12%	26%
1.6	1185	10%	23%
1.8	1324	11%	24%
2.0	1231	10%	22%

TABLE 3. Results of the conditional sampling and averaging: N_b, number of burst events; N_s, number of sweep events; T_b, total period of burst events, i.e. $N_b \tau_d$; T_s, total period of sweep events, i.e. $N_s \tau_d$; uw_b, total Reynolds stress caused by the burst events, i.e. $\Sigma_{j=1}^{N_b} (uw_b)_j$; uw_s, total Reynolds stress caused by the sweep events, i.e. $\Sigma_{j=1}^{N_s} (uw_s)_j$; T, total data length (300 s); uw, total Reynolds stress, i.e. $\int_0^T u(t)\,w(t)\,dt$; $\overline{uw}$, local Reynolds stress, i.e. uw/T; C, threshold level for the detection of events, $10\overline{uw}$; τ_d, duration of the event.

the water surface, further analyses were done using the same data as are partly shown in figure 3 (fetch = 6 m, wind speed U_1). We examined the velocity fluctuations $(u(t), w(t))$ obtained at heights $z = 1.2$, 1.4, 1.6, 1.8 and 2.0 cm in the lower part $(0.15-0.3\delta)$ of the logarithmic boundary layer. Five-minute data of the velocity fluctuations and surface displacement just under the hot wire were analysed. Conditional sampling and averaging techniques were used to quantify the contribution of the bursting phenomena to the Reynolds-stress production. A scheme for recognition of the bursting phenomena over wind waves was determined based on the results of KOKT summarized above.

The signals of $u(t)\,w(t)$ have been used to detect the bursts and sweeps: the appearance of an $u(t)\,w(t)$ value that exceeds a threshold level C toward the negative, specifies the occurrence of the bursting phenomena, and a coupling of plus or minus in $u(t)$ and $w(t)$ designates a burst or sweep, i.e. if $u < 0, w > 0$, it is a burst, and if $u > 0, w < 0$, a sweep. A value ten times the Reynolds stress $-\overline{uw}$ at each measurement height was employed as the threshold C after some trial analyses using the data from the lowest height. However, since the heights of the analysed cases are within the constant-momentum-flux layer (figure 3), the threshold values are nearly constant (table 3). To define a time average, a duration period for the bursting phenomena τ_d has been set: a period is chosen during which a flow pattern with one wind-wave lengthscale (10.5 cm, calculated from $f_p = 3.86$ Hz in table 1) passes through a fixed point with an approximate mean horizontal velocity at these heights $(U = 4.0$ m/s at $z = 1.2$ cm was employed here). The reasons for this choice are: (1) the FD ordered motion, which indicates the active interactions with the under layers,
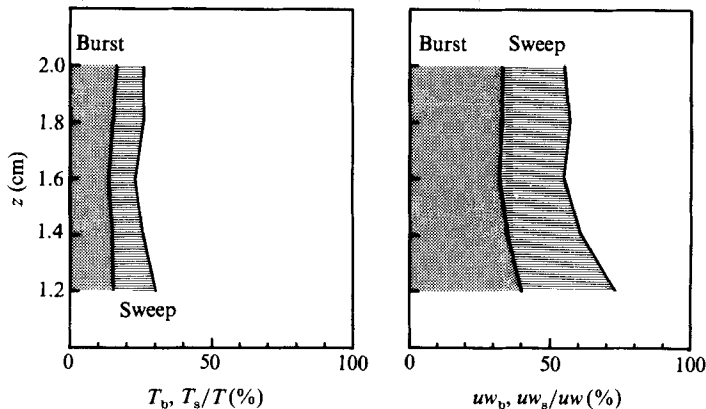
FIGURE 25. (a) Total periods of the burst and the sweep expressed as a percentage of the total period, and (b) the Reynolds stress produced by the burst and the sweep as a percentage of the total Reynolds stress.

has a characteristic horizontal lengthscale of one wind-wave length; and (2) the 'big burst' hypothesized is related to the separation bubble and the remarkably rapidly growing ordered motion, both of which have a scale of one wind-wave length.

Details of the sampling and averaging processes are: (1) a time t_c, when a value $u(t)\,w(t)$ exceeding C appears, is detected by scanning through the signals from the start; (2) a time when the minimum value of $u(t)\,w(t)$ occurs in a period $t_c - \tau_d/2 < t < t_c + \tau_d/2$, is searched for and then defined as the new t_c; (3) Reynolds stress caused by the jth burst or sweep is obtained from the integral

$$(uw_i)_j = \int_{t_c-\tau_d/2}^{t_c+\tau_d/2} u(t)\,w(t)\,\mathrm{d}t, \quad i = \mathrm{b\ or\ s}; \qquad (6.1)$$

(4) for each of the events, the position relative to an underlying wind wave is obtained. If the signals $u(t)$ and $w(t)$ are used in the integral (6.1),they are replaced by zero. Therefore, no signal is used more than once in this analysis. Overlapping of two successive events sometimes took place, but the total periods of overlapping were only a few per cent of the total period of the bursting phenomena. Therefore, we have neglected the effect of overlapping on the calculation.

6.2. Results

Table 3 shows, for each of the cases, the number of wind waves and the numbers, total periods and total contributions to the Reynolds stress of the burst and sweep events. When the hot wire was placed at $z = 1.2$ cm (the lowest height), 73% (40% from the burst and 33% from the sweep) of the local Reynolds stress was produced by the bursting phenomena during 30% (17% from the burst and 13% from the sweep) of the total period. The periods and contributions of the bursting phenomena for all the heights are illustrated in figure 25. For the greater heights, about 60% of the local Reynolds stress was caused by the bursting phenomena during 25% of the total period. The reason for the high detection rate of the contribution for the lowest height may be that we determined the values of τ_d using U at this height. If we chose the parameters for the recognition and calculation scheme carefully, the detection rate may increase.
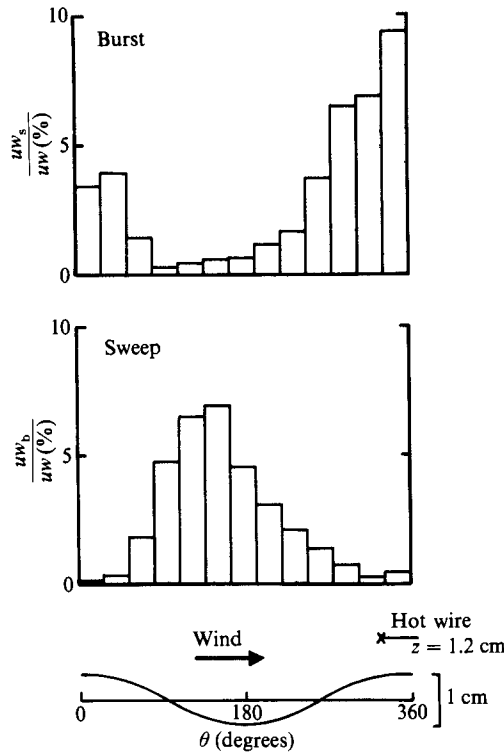
FIGURE 26. Distribution of the Reynolds-stress production caused by a burst and sweep relative to the wind-wave phase. The hot wire was at $z = 1.2$ cm.

Table 3 also shows that the numbers of burst and sweep events (N_b and N_s) are greater than the number of wind waves for every height. When we consider in §7 the mechanisms that are consistent with all the aspects of the turbulent boundary layer revealed in the present study, the comparison of these numbers will become important.

Figure 26 shows the distribution of the Reynolds-stress production by a burst and sweep relative to the wind-wave phase at $z = 1.2$ cm. As pointed out by KOKT, a burst occurs at positions close to the crest over the windward side. This analysis reveals that a sweep occurs over the leeward side of the trough ($\theta = 90°$–$180°$). The relation between the bursting phenomena and the wind-wave phase does not change as much for the other heights. The bursting phenomena over wind waves produce a major portion of the Reynolds stress in the lower logarithmic boundary layer, just as over flat plates. However, their occurrence has a close relation to the underlying wind waves, as will be discussed in the following section.

7. Discussion

7.1. *Interaction mechanisms between the air flow and wind waves*

As shown in §5 and also as reported by Kawa (1981, 1982), two distinct air-flow structures, with and without separation, exist under the conditions of our experiment, where breaking with air bubble entrainment did not occur. A significant frequency of occurrence of each of the structures suggests that air-flow separation is

an aspect inherent in wind waves. In order to understand the dynamical roles of the separated shear flow over wind waves, we briefly review some experimental results associated with turbulent flow structure, including separation and reattachment.

'Backward facing' steps have often been employed to study such a flow structure because of their simple geometry and practical benefits experimentally (for example, Tani, Iuchi & Komoda 1961; Bradshaw & Wong 1972). Tani *et al.* have shown evidence of much activity in turbulent shear stress generation in the separated shear layer. The shear stress and the turbulence intensity increase with distance from a separation point, and their maxima appear near the reattachment region. Tani *et al.* measured wall pressure and found a rapid pressure rise caused by the reattachment of the separated turbulent shear flow. The pressure rise was universally observed in the reattachment region, regardless of step height and conditions in the boundary layer before the separation. They have suggested that the pressure exerted by the solid surface is balanced by the turbulent shear stress set up by its own kinematics, i.e. the shear instability mechanism in the separated shear layer.

Bradshaw & Wong (1972), who also gave a broad review of previous experimental studies on flow separation and reattachment, measured wall-surface shear stress and showed that the surface stress rose rapidly after reattachment. On the basis of the Tohoku University Group's work on wind waves (especially Okuda *et al.* 1977; Okuda 1982 a–c; and Kawai 1982) Csanady (1985) has pointed out the dynamical consistency of this shear-stress rise and the shear-stress spike just upstream of the wave crest that was first documented by Okuda *et al.* (1977).

Zilker & Hanratty (1979) and Buckles, Hanratty & Adrian (1984) have examined flow separation over a solid sinusoidal wave surface and given a detailed description of the properties near the reattachment region. When we define the phase θ of the sinusoidal surface as $\theta = 0°$ for a wave crest causing flow separation and $\theta = 360°$ for the next downstream-wave crest, the separated shear flow was observed to reattach to the surface at about $\theta = 250°$. Pressure rise at the wall was investigated at $\theta = 270°$, and a wall shear-stress spike at $\theta = 316°$ was found. Downstream of the reattachment point (near the shear-stress maximum) the mean streamlines were lifted and compressed in response to the lifting wave surface; this feature is a particular difference between a sinusoidal wall boundary and the backward-facing steps (Buckles *et al.* 1984). These compressed streamlines indicate that there is a significant accelerated flow that can be considered to make the shear-stress spike more prominent than it is for backward-facing steps.

Using the pattern of air-flow separation shown in figure 13 of Kawai (1982), Csanady (1985) compared the sharp-crested wavelets to the backward-facing step. To discuss the location of the reattachment of the separated shear flow over wind waves, he adopted a three-dimensional, rather two-dimensional, separating flow pattern over wavelets. However, the figure 13 of Kawai (1982) has been replaced by figure 23 in the present study. The results of Buckles *et al.* (1984) showed a two-dimensional separating flow pattern over a sinusoidal wall, which has a strong similarity to the present experimental results. The three-dimensional nature of air-flow separation suggested by Csanady (1985) may become effective over an open water surface.

The separated shear layer over wind waves reattaches to the preceding wave surface at about $\theta = 260°$, as shown in figure 23. Therefore, if we assume that reattachment has the same effect on the water surface as on a wavy wall, the position of the shear-stress spike expected from the results of Buckles *et al.* agrees with that found by Okuda *et al.* (1977) and Okuda (1982 a). A pressure rise can be predicted

near the region of downward motion of water particles at the surface ($\theta = 280°$), but it has not been measured. The resulting asymmetrical distribution of pressure along the wave surface can feed energy into wind waves.

Using an artificially induced stationary breaking wave, Banner (1986) has measured the surface pressure distribution over breaking waves for a range of u_*/C of approximately 0.2–0.4. He has shown a large asymmetry in the local surface pressure distribution. This can be considered as showing the effect on the surface pressure distribution of the separated turbulent shear flow which has been described in the present study.

The two alternative regimes of the flow structure (with and without air-flow separation) should be noted when we examine the effects of reattachment on wind waves. Since the wind-wave field is statistically steady, it is reasonable to suppose that, when we follow a wind wave, we observe both of the flow structures over the wave, i.e. a beginning stage and an end stage of air-flow separation. Okuda (1982b) has shown that a distinct high-vorticity region near the wave crest, which is associated with the shear-stress spike just upstream of the crest, grows and attenuates systematically while the wave is travelling. When air-flow separation begins, the expected shear stress may start to form the high-vorticity region and thicken it with time. Okuda (1984) dealt with this process numerically. It is suggested that dynamical interaction mechanisms between the air flow and wind waves need to be dealt with as a time-dependent problem.

7.2. 'Big burst' model

In this subsection and the next we consider the mechanisms of the bursting phenomena investigated in the layer 0.15δ–0.3δ with emphasis on the ordered motion in the upper layer (0.4δ–1δ) and the air-flow separation in the lower layer (0–0.15δ). In the turbulent boundary layer over flat plates, low-speed fluid, which bursts upward and is related to large-scale ordered motion, originates from the streaky structure near the viscous sublayer. On the other hand, the bursting phenomena over wind waves have a specific relationship with the wind-wave phase as shown in figure 26. The source of the low-speed fluid near the water surface could be the separation bubble. The low-speed fluid inside the bubble covers the trough region, and energetic turbulence is generated in the separated shear layer at the outer edge of the bubble.

An alternative property of the flow structure was noted in the previous subsection: the end stage of the air-flow separation is introduced to explain the bursting phenomena; that is, the 'blowing-up' of all the fluid in the separation bubble may be the burst and the compensating flow to the vacated area after that may be the sweep. A schematic picture illustrates this model in figure 27: (a) it starts from the flow structure that includes the separation bubble; (b) when the local gradient of the wave surface causing the separation disappears, the air mass in the bubble starts to move downward and a supplementary flow comes in to replace this; (c) the air mass progresses up the slope of the preceding crest, being accelerated and gaining an upward velocity component; and (d) it blows-up over the windward side of the wave. As shown in figure 24, a hot wire placed at a position just above the crest level detects the ascending low-speed air mass ($u < 0, w > 0$) over the windward side and the descending high-speed air mass ($u > 0, w < 0$) over the leeward side. Hereafter, we call this model 'big burst'. It is a transient event from a flow structure with separation to one without separation.

Kawai (1982) observed a prominent phenomenon, which was the blowing-up of a
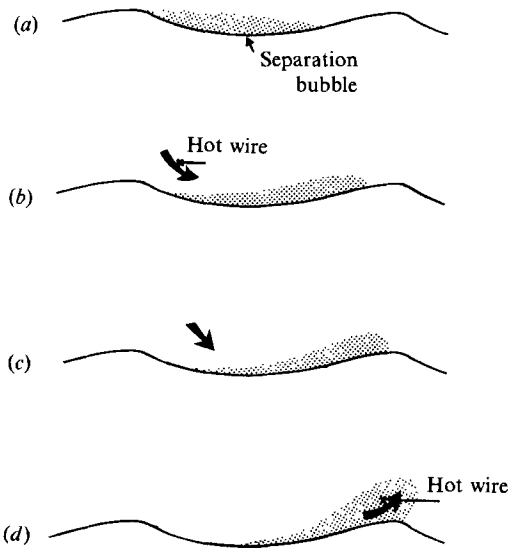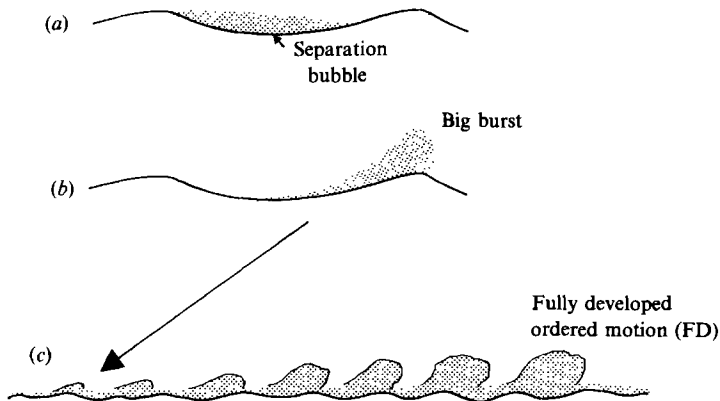
FIGURE 27. 'Big burst' model (see the text).

FIGURE 28. A model connecting the big burst and the rapidly growing ordered motion.

considerable mass of low-speed air (his figure 7e) producing a large Reynolds stress (his figure 9). This may be the visualized 'big burst'.

We can connect the blowing-up of the air mass of the big burst with the remarkable growth of the ordered motion in the outer boundary layer, as shown in figure 15. This ordered motion was observed to increase in height from approximately the outer edge of the inner layer ($\sim 0.4\delta$) to the height of the boundary layer ($\sim 1\delta$), keeping the horizontal lengthscale of one wavelength. As shown by the results of the conditional sampling for the bursting phenomena, the low-speed fluid goes upward through the layer 0.15δ–0.3δ. It can be inferred generally that the low-speed fluid becomes turbulent while it is being blown up. To explain the model connecting the big burst and the growing ordered motion, a schematic picture is shown in figure 28. This indicates how the low-speed air mass in the separation bubble, which has an original lengthscale of one wavelength, is blown up (the big burst, figures 28a, b) and

then this air mass increases its height, becoming turbulent without losing its identity as it travels downstream (figure 28c).

It is known that, in the separation bubble, there exists a rotating flow coming from the reattachment region and directed upstream (relative to the basic flow) along the bottom boundary. This flow was also investigated over wind waves by Kawai (1982). Vorticity, distributed in the whole separation bubble due to this flow, might be important in maintaining its identity after the bursting occurs. It can be noted that the FD ordered motion possesses a slow vortical motion, in the same sense as the separation bubble, as described in §4.

According to Kawai (1982)'s statistics on the frequency of different air-flow structures, both of the two flow structures, with and without separation, can be considered to be stable because of their frequent appearance. However, the blowing-up of the low-speed air mass, which we regard as the big burst, was rarely observed. If the flow structure with separation is stable, the rare occurrence of its end stage (the big burst) is reasonable. In §6, we noted that the occurrence of both the burst and sweep is greater than the number of wind waves passing through the observation point. Since we do not expect so many occurrences of the big burst, we need to consider another mechanism to explain most of the bursting phenomena.

7.3. 'Small burst' model

The FD ordered motion moves downstream with approximately the free-stream velocity. Since the free-stream velocity is much faster than the phase velocity of wind waves, a number of the FD ordered motions can pass through a measurement point while one wind wave does so. Hence if the FD ordered motion interacts with the inner boundary layer to cause the bursting phenomena, we can explain why the number of bursting phenomena exceeds the number of wind waves. We have shown that the low-speed fluid with upward velocity produces a large Reynolds stress inside the upstream edge of the FD and the high-speed air goes downward at the streamwise interface. This investigation indicates the existence of interaction with the near-surface layers.

We have concluded from a number of experimental investigations including our own that energetic turbulence is generated in the separated shear layer. When we assume that this energetic turbulent air mass blows up from the unstable reattachment region, its appearance will be the burst, i.e. the blowing-up of the low-speed air mass on the windward side of the wind waves.

By relating the FD ordered motion to the turbulence generated in the separated shear layer it is possible to propose another mechanism for the bursting phenomena, called 'small burst'. However, the small-burst model is more speculative than the big burst because less is known about the connection between the FD and the inner boundary layer. With the aid of the series of sketches shown in figure 29, the small-burst model can be explained: when the FD ordered motion passes over the separation bubble, its original motion influences the separated shear layer (the ordered motions at the left of a) and it sucks the energetic turbulent eddies from the reattachment region (c and d). The FD maintains its rotating motion and its turbulence by means of entrained eddies (e). The sweep seems to be related to the high-speed air coming down at the streamwise interface of the FD (c), but this is as yet unknown. As shown in (c), the horizontal lengthscale equal to one wavelength of the ordered motions forming a train might be important since, to preserve air mass conservation for the blowing-up in the form of a small burst, the specified spacing between successive ordered motions may provide supplementary fluid to the
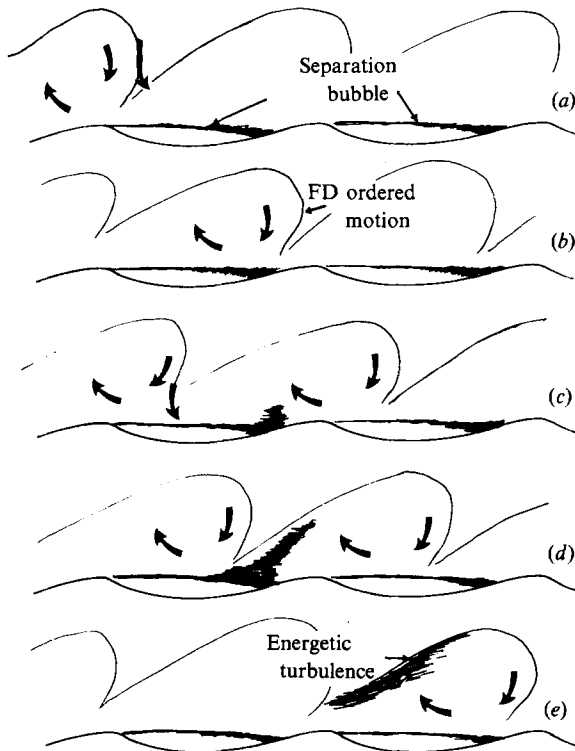
FIGURE 29. 'Small burst' model (see the text).

separated shear layer, contributed by the sweep. The observation that the horizontal lengthscale of the ordered motions corresponds approximately to the wavelength of the underlying wind waves might be explained by the existence of a kind of resonant interaction between a train of the ordered motions in the air flow and the underlying wind-wave train, which is growing downstream. That is, if the successive ordered motions interact with the separation bubble as described in the small-burst model, the spacing of the bulge might be adjusted to the wavelength since the size and spacing of the separation bubbles are determined by the wavelength of wind waves.

REFERENCES

BANNER, M. L. 1986 The influence of wave breaking on the surface pressure distribution in wind-wave interactions. Applied Mathematics Preprint. AM86/9, The University of New South Wales.

BANNER, M. L. & MELVILLE, W. K. 1976 On the separation of air flow over water waves. J. Fluid Mech. 77, 825–842.

BANNER, M. L. & PHILLIPS, O. M. 1974 On the incipient breaking of small scale waves. *J. Fluid Mech.* **65**, 647–656.

BLACKWELDER, R. F. & KOVASZNAY, L. S. G. 1972 Time scales and correlations in a turbulent boundary layer. *Phys. Fluids* **15**, 1545–1554.

BRADSHAW, P. & WONG, F. Y. F. 1972 The reattachment and relaxation of a turbulent shear flow. *J. Fluid Mech.* **52**, 113–135.

BROWN, G. L. & THOMAS, A. S. W. 1977 Large structure in a turbulent boundary layer. *Phys. Fluids* **20**, S243–252.

BUCKLES, J., HANRATTY, T. J. & ADRIAN, R. J. 1984 Turbulent flow over large-amplitude wavy surface. *J. Fluid Mech.* **140**, 27–44.

CANTWELL, B. J. 1981 Organized motion in turbulent flow. *Ann. Rev. Fluid Mech.* **13**, 457–515.

CHAMBERS, A. J. & ANTONIA, R. A. 1981 Wave-induced effect on the Reynolds shear stress and heat flux in the marine surface layer. *J. Phys. Oceanogr.* **11**, 116–121.

CHANG, P. C., PLATE, E. J. & HIDY, G. M. 1971 Turbulent air flow over the dominant component of wind-generated water waves. *J. Fluid Mech.* **47**, 183–208.

CORINO, E. R. & BRODKEY, R. S. 1969 A visual investigation of the wall region in turbulent flow. *J. Fluid Mech.* **37**, 1–30.

CSANADY, G. T. 1985 Air–sea momentum transfer by means of short-crested wavelets. *J. Phys. Oceanogr.* **15**, 1486–1501.

FALCO, R. E. 1977 Coherent motions in the outer region of turbulent boundary layers. *Phys. Fluids* **20**, S124–132.

GRASS, A. J. 1971 Structural features of turbulent flow over smooth and rough boundaries. *J. Fluid Mech.* **50**, 233–255.

HATORI, M. 1984 Nonlinear properties of laboratory wind waves at energy containing frequencies. Part 1. Probability density distribution of surface elevation. *J. Oceanogr. Soc. Japan* **40**, 1–11.

KAWAI, S. 1981 Visualization of airflow separation over wind-wave crests under moderate wind. *Boundary-Layer Met.* **21**, 93–104.

KAWAI, S. 1982 Structure of air flow separation over wind-wave crests. *Boundary-layer Met.* **23**, 503–521.

KAWAMURA, H., OKUDA, K., KAWAI, S. & TOBA, Y. 1981 Structure of turbulent boundary layer over wind waves in a wind wave tunnel. *Tohoku Geophys. J. (Sci. Rep. Tohoku Univ.* Ser. 5) **28**, 69–86.

KIM, H. T., KLINE, S. J. & REYNOLDS, W. 1971 The production of the wall region in turbulent flow. *J. Fluid Mech.* **50**, 133–160.

KLINE, S. J., REYNOLDS, W. C., SCHRAUB, F. A. & RUNSTADLER, P. W. 1967 The structure of turbulent boundary layers. *J. Fluid Mech.* **30**, 741–773.

KOVASZNAY, L. S. G., KIBENS, V. & BLACKWELDER, R. 1970 Large scale motion in the intermittent region of a turbulent boundary layer. *J. Fluid Mech.* **41**, 283–325.

LAUFER, J. 1975 New trends in experimental turbulence research. *Ann. Rev. Fluid Mech.* **7**, 307–326.

LESSEN, M. 1950 On stability of the free laminar boundary layer between parallel streams. *NACA Rep.* 979.

OKUDA, K. 1982*a* Internal flow structure of short wind waves. Part I. On the internal vorticity structure. *J. Oceanogr. Soc. Japan* **38**, 28–42.

OKUDA, K. 1982*b* Internal flow structure of short wind waves. Part II. The streamline pattern. *J. Oceanogr. Soc. Japan* **38**, 313–322.

OKUDA, K. 1982*c* Internal flow structure of short wind waves. Part III. Pressure distributions. *J. Oceanogr. Soc. Japan* **38**, 331–338.

OKUDA, K. 1984 Internal flow structure of short wind waves. Part IV. The generation of flow in excess of the phase speed. *J. Oceanogr. Soc. Japan* **40**, 46–56.

OKUDA, K., KAWAI, S. & TOBA, Y. 1977 Measurements of skin friction distribution along the surface of wind waves. *J. Oceanogr. Soc. Japan* **33**, 190–198.

TAKEUCHI, K., LEAVITT, E. & CHAO, S. P. 1977 Effects of water waves on the structure of turbulent shear flows. *J. Fluid Mech.* **80**, 535–559.

TANI, I., IUCHI, M. & KOMODA, H. 1961 Experimental investigation of flow separation associated with a step or a groove. *Aero. Res. Inst. Univ. Tokyo Rep.* 364, pp. 119–137.

TATSUMI, T. & GOTOH, K. 1960 The stability of free boundary layers between two uniform streams. *J. Fluid Mech.* 7, 433–441.

TOBA, Y. 1972 Local balance in the air–sea boundary processes, I. On the growth process of wind waves. *J. Oceanogr. Soc. Japan* 28, 109–120.

TOBA, Y. 1973 Local balance in the air–sea boundary processes, III. On the spectrum of wind waves. *J. Oceanogr. Soc. Japan* 29, 209–220.

TOBA, Y. 1978 Stochastic form of the growth of wind waves in a single parameter representation with physical implications. *J. Phys. Oceanogr.* 8, 494–507.

TOBA, Y., TOKUDA, M., OKUDA, K. & KAWAI, S. 1975 Forced convection accompanying wind waves. *J. Oceanogr. Soc. Japan* 31, 192–198.

WEISSMAN, M. A. 1981 Observations and measurements of air flow over water waves. In *Wave Dynamics and Radio Probing of the Ocean Surface* (ed. O. M. Phillips & K. Hasselmann), pp. 335–352. Plenum.

ZILKER, D. P. & HANRATTY, T. J. 1979 Influence of the amplitude of a solid wavy wall on a turbulent flow. Part 2. Separated flows. *J. Fluid Mech.* 90, 257–271.